Article:
Gallagher, C., Butcher, F.E.G., Balme, M. et al. (2021) Landforms indicative of regional warm based glaciation, Phlegra Montes, Mars. Icarus, 355. 114173. ISSN: 0019-1035

https://doi.org/10.1016/j.icarus.2020.114173

Icarus xxx (xxxx) xxx

Contents lists available at ScienceDirect

Icarus

journal homepage: www.elsevier.com/locate/icarus

Research Paper

Landforms indicative of regional warm based glaciation, Phlegra Montes, Mars

Colman Gallagher [a,b,*], Frances E.G. Butcher [c], Matt Balme [d], Isaac Smith [e,f], Neil Arnold [g]

[a] UCD School of Geography, University College, Dublin D04 V1W8, Ireland
[b] UCD Earth Institute, University College, Dublin D04 V1W8, Ireland
[c] Department of Geography, University of Sheffield, Sheffield S10 2TN, UK
[d] The Open University, School of Physical Sciences, Walton Hall, Milton Keynes, MK7 6AA, UK
[e] Department of Space Studies, Southwest Research Institute, Boulder, CO 80302, USA
[f] Planetary Science Institute, Tucson, AZ 85719, USA
[g] Scott Polar Research Institute, Cambridge, UK

ARTICLE INFO

Keywords:
Mars
Glaciers
Warm-based glaciation
Water

ABSTRACT

Viscous flow features (VFF) occur in the mid-latitudes of Mars and have characteristics consistent with being glaciers. Climate models suggest that martian glaciers are cold-based systems in which meltwater has never been widely produced. VFF are common in Phlegra Montes, a mountain range in the mid-latitudes of the northern hemisphere of Mars. However, in Phlegra Montes, the presence of an esker associated with an extant Amazonian Period VFF provides evidence that warm-based glacial processes did formerly operate. The problem at the centre of this paper is that the glacial meltwater responsible for this esker could have been produced as a consequence of its setting in a graben, with locally enhanced geothermal heating having been the driver of melt, not systemic heating associated with a regional warm-based regime. Given this uncertainty, this paper aims to determine if there are indicators of more widespread warm-based glacial processes in Phlegra Montes. The paper briefly describes the distribution and characteristics of VFF across the region, before focussing on the search for key landforms considered diagnostic of erosion by warm-based glaciers. From our observations, including discriminant morphometrics, we conclude that the landscape of Phlegra Montes is indicative of widespread warm-based glacial processes, including subglacial scour, linear abrasion and the incision of subglacial meltwater channels. Our findings have significance in constraining the contexts and process environments within which liquid water has been produced during the Amazonian Period on Mars and point to several lines of future research into martian glaciation, climate and landscape evolution.

1. Introduction

Phlegra Montes are a mountain complex on Mars extending NNE-SSW, over ~1000 km, between latitudes 30° - 52° N (Fig. 1). The region is dominated by two uplands of Hesperian-Noachian transition age (Tanaka et al., 2014; Fig. 1), composed of impact breccias, sediments and volcanic deposits. The uplands are separated by low-lying Hesperian-Amazonian flood lavas and lava flows (dated locally to 1.6 ± 0.1 Ga by Gallagher and Balme, 2015), and bordered by Hesperian sedimentary units and isolated Noachian highland remnants (Tanaka et al., 2014). The uplands are characterised by rounded, dome-like mountains, with intervening valleys and basins, some of which are occupied by viscous flow features (VFF) of different types (e.g. Fig. 2, Appendix S1). Characteristic ridges, troughs and lobes of the VFF (Milliken et al., 2003) suggest that these are glaciers (Souness et al., 2012; Hubbard et al., 2014), which can be classified further based on form and topographic context. Commonly, low plains bounding mid-latitude uplands on Mars are characterised by lobate debris aprons (LDA; Squyres, 1979; Carr, 2006), which are accumulations of ice mantled by lithic debris, including dust (Kochel and Peake, 1984; Pierce and Crown, 2003; Holt et al., 2008; Plaut et al., 2009; Parsons et al., 2011; Fastook et al., 2014; Baker and Head, 2015; Petersen et al., 2018). Mid-latitude valleys within uplands on Mars are commonly occupied by lineated valley fills (LVF; Head et al., 2006), which closely resemble valley glaciers on Earth. In Phlegra Montes, several LDA are fed by higher LVF, creating composite systems. Viscous, concentric crater fills (CCF; Dickson et al.,

* Corresponding author at: UCD School of Geography, University College, Dublin D04 V1W8, Ireland.
E-mail address: colman.gallagher@ucd.ie (C. Gallagher).

https://doi.org/10.1016/j.icarus.2020.114173
Received 30 January 2020; Received in revised form 19 September 2020; Accepted 13 October 2020
Available online 20 October 2020

2009) are common in the region. The crater retention ages of martian mid-latitude VFF indicate that they formed over the past 1 Gy (Fassett et al., 2014; Baker and Head, 2015), most recently over the last ~0.6 Gy, in the Late Amazonian epoch (Milliken et al., 2003; Hubbard et al., 2011; Souness et al., 2012; Hubbard et al., 2014). Dating by Gallagher and Balme (2015) of the VFF referred to in this paper as LVF 393 (Fig. 1, Fig. 2a, Appendix S1) places it also into the Amazonian, with a crater retention age of 150 ± 20 Ma, although this is probably a very approximate age; the few larger craters on LVF 393 might follow an older isochron, still Amazonian, but on the order of 1–1.5 Ga.

As the majority of Amazonian VFF are considered to have been cold/dry based or minimally polythermal glaciers (Hubbard et al., 2011; Hubbard et al., 2014), the dynamics of these systems are believed to have been dominated by creep (Milliken et al., 2003; Parsons et al., 2011). Warm-based sliding, required to produce the regional-scale landscapes associated with widespread glacial erosion so common on Earth (Sugden, 1974; Glasser and Bennett, 2004), is not predicted to have occurred widely in recent martian environments. Although Conway et al. (2018) concluded that widespread melt of crater wall glaciers occurred 5–10 Ma, observations of landforms, in contextually consistent landsystems (Eyles, 1983) diagnostic of warm/wet based glacial regimes on Mars, especially eskers (Close, 1867), are rare in comparison to the widespread presence of VFF (Souness et al., 2012; Levy et al., 2014). However, Gallagher and Balme (2015) identified an esker in Phlegra Montes, emerging from the distal deposits of a glacial landsystem morphologically integrated with LVF 393 (Fig. 1). Given the wide consensus on the dominance of cold/dry-based mid-latitude glaciation on Mars, the conclusion was that the Phlegra Montes esker represents the former occurrence of spatially limited warm-based conditions, associated with enhanced geothermal heating along the graben in which the esker is located. Thermal modelling by Butcher et al. (2017) of a glacier-linked esker in a similar setting in northwestern Tempe Terra indicates that elevated geothermal heat flux and viscous strain heating could have permitted restricted wet-based glaciation, even in a general environment in which climate was too cold for more extensive wet-based process environments. These conclusions raise the question at the core of this paper; is the esker in Phlegra Montes an extremely rare exception to a cold/dry-based norm - or did warm/wet-based VFF exist more widely across the region? In answer to this question, the paper first describes the extant VFF in Phlegra Montes, including a determination of the thickness and composition of one of the largest, with estimates of the properties of several others. The focus of the paper, however, is to determine if the landscape context of these VFF provides evidence of widespread warm-based processes. This is done by reference to geomorphological criteria diagnostic of warm based glacial processes on Earth (Table 1), identified principally by Glasser and Bennett (2004). The paper describes candidate analogues of these key terrestrial landforms and discusses the implications of their occurrence in Phlegra Montes with respect to former subglacial thermal regime. Contextualization of the extant VFF within this geomorphological framework provides valuable insights to the evolution of glaciation in the region.

2. Data

Landforms were mapped and measured from mosaicked CTX (Context Camera, NASA Mars Reconnaissance Orbiter; Malin et al., 2007; image credits: NASA/JPL-Caltech/MSSS) visible-wavelength images (resolution ~6 m per pixel), displayed in an equirectangular projection. To preclude projection-induced distortions, all directions were measured relative to true north and all spatial measures were geodesic. CTX images were overlaid in a Geographic Information System (GIS) onto the MOLA-HRSC Blended Global 200 m/pixel digital elevation model (DEM) v2

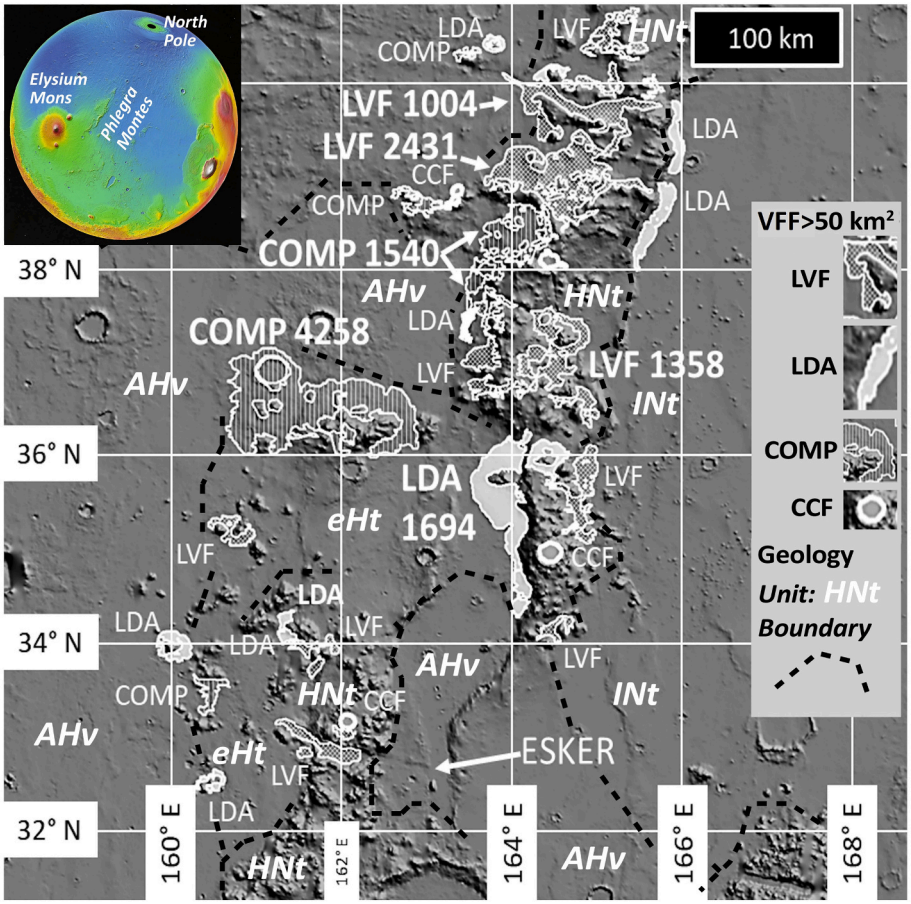

Fig. 1. Extant VFF and shaded relief of Phlegra Montes with main geological units and boundaries (after Tanaka et al., 2014): *lNt*, late Noachian transition; *HNt*, Hesperian-Noachian transition; *eHt*, early Hesperian transition; *AHv*, Amazonian-Hesperian volcanic. Elevation data Mars Orbiter Laser Altimeter (MOLA)/ USGS 463 m global mosaic. Crosshatch fill = LVF; light grey fill, thin edge = LDA; vertical cross hatch, thin edge = compound LVF-LDA (COMP); light grey fill, thick edge = CCF. Arrow shows location of the esker associated with LVF 393, described by Gallagher and Balme (2015). Labels with numbers refer to the type and surface area (km^2) of the largest VFF. Note the lack of VFF in summital areas, e.g. east of LDA 1694 and along the northern mountain spine, east of COMP 1540. MOLA data credit: USGS, NASA, JPL.

(Fergason et al., 2018), derived from Mars Orbiter Laser Altimeter (MOLA; Smith et al., 2001) and High-Resolution Stereo Camera (HRSC; Neukum et al., 2004) data. Elevation profiles were plotted from digital elevations models (DEM) based on HRSC elevation data (50 m/pixel) or (where available) High Resolution Imaging Science Experiment (HiRISE; McEwen et al., 2007) elevation data (DEM at 2 m/pixel). Only meso-scale to macro-scale landforms (>20 m to 1 km) are widely considered in the observations that follow, although HiRISE images and anaglyphs were used, where available and relevant, to describe and measure smaller landforms. To confirm that the VFF are composed of ice, rather than being lithic or volcanic valley-fills (cf. Byrne et al., 2013) determinations of VFF ice content, purity and total thickness were attempted using data from the Mars Reconnaissance Orbiter (MRO) Shallow Radar instrument (SHARAD, Seu et al., 2007; Appendix S2.1). Owing to topographic clutter, these determinations were possible for only one VFF. However, the average thickness of this VFF and several others was estimated (Appendix S2.2) and complementary determinations of its surface properties were made (Appendix S2.3).

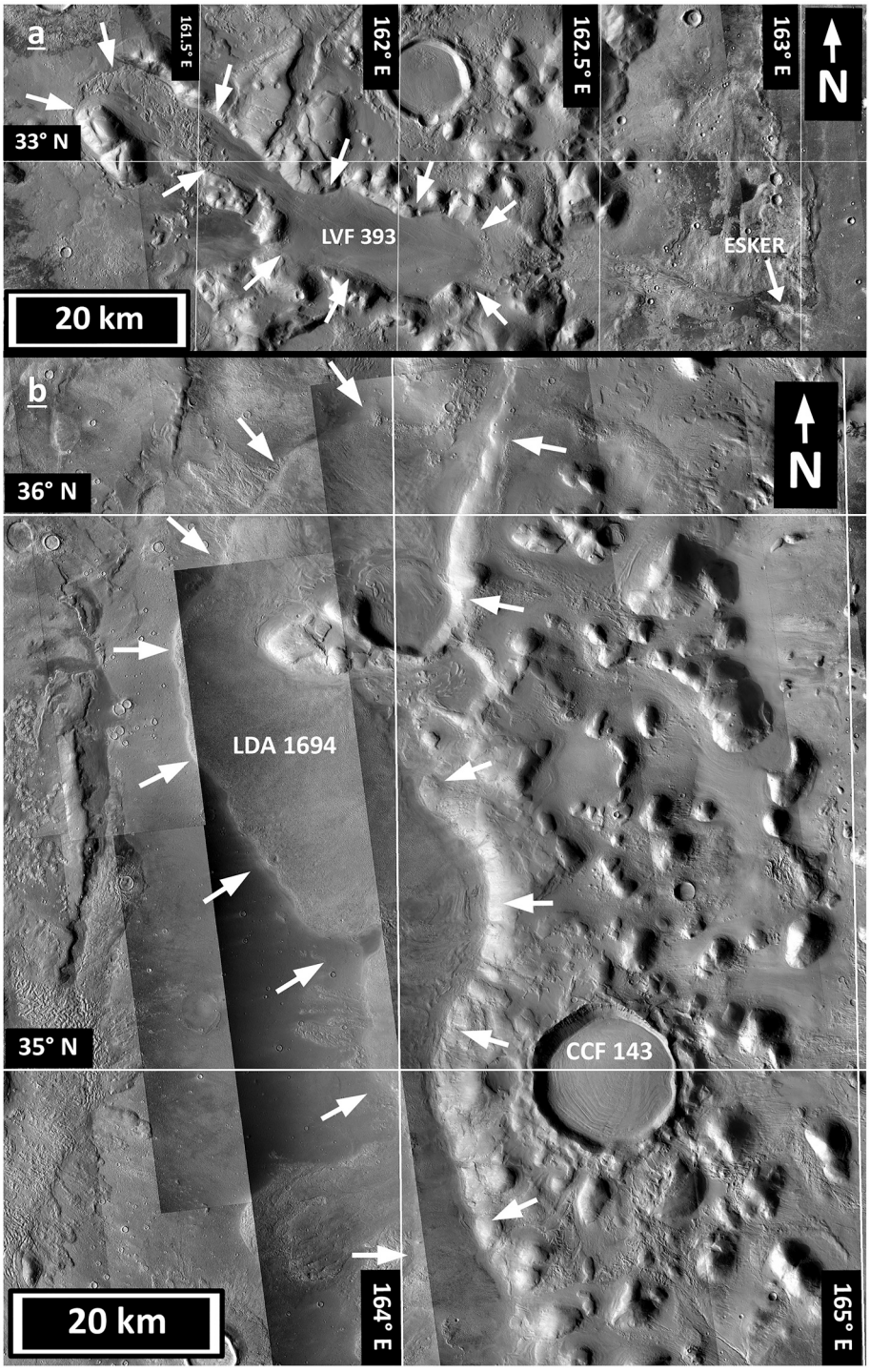

Fig. 2. The VFF exceeding 50 km^2 (VFF > 50) in Phlegra Montes are mainly LVF (panel a), LDA and CCF (panel b), with some COMP systems (Appendix S1 provides areo-referenced shapefiles of the VFF > 50). (Panel a) LVF 393 (margin indicated by arrows) and esker, occupying part of a long graben. CTX mosaic: B01_010005_2122; B05_011706_2116; P18_007935_2132. CTX image credits: NASA/JPL/MSSS. (Panel b) LDA 1694 (margin indicated by arrows) occupies part of the basin between the northern and southern mountain spines of Phlegra Montes. The crater east of LDA 1694, catalogued in the Robbins Crater Database (RCD) as RCD 07–000133 (Robbins and Hynek, 2012) is occupied by CCF 143. CTX mosaics: (Panel a) P22_009794_2155; B17_016163_2147; (Panel b) P16_007368_2152; P16_007368_2152; B16_015886_2177; P21_009161_2167; P21_009161_2167; P14_006656_2169; P17_007658_2175. CTX image credits: NASA/JPL/MSSS.

Table 1
Landforms and values of morphometric parameters considered diagnostic of erosion by warm-based glacial ice (after Glasser and Bennett, 2004; Galofre et al., 2018; Bouquety et al., 2019), with cross-referencing to figures showing candidate examples in Phlegra Montes (see Appendix S2.4 for location map of candidate landforms).

Landform	Process context	Geomorphology/context	Diagnostic morphometric	Figure
Zones of areal scour	Bedrock abraded by basal glacial debris	Streamlined meso-scale assemblages of stoss-and-lee forms and rock basins		4
Glacial troughs	Bedrock overdeepening by linear (rather than areal) glacial erosion	Topographically constrained valley glaciers, outlet glaciers or ice sheets	*V-index* > 0	5, 6
Corries (cirques)	Overdeepening by freeze-thaw weathering and glacial plucking	Bedrock hollows	*L:W* ~ 1, *W:H* ~ 2.7	5, 7 (Appendix S2.5, S2.6)
Giant (10^2–10^3 m) to meso-scale stoss and lee forms (*roches moutonnées*)	Stoss-side smoothing by abrasion, lee-side quarrying by plucking	Bedrock with gently sloping stoss-side and a steeper, rougher lee-side		Appendix S2.7
Lee-side rock cavities/basins, 10^0–10^2 m-scale	Plucking of joints and other weaknesses (joint exploitation) in subglacial cavities on the lee-side of bedrock protuberances	Bedrock weaknesses (jointing or other structural elements)		8 and Appendix S2.8
Meso-scale streamlined bedrock forms	Glacial abrasion of meso-scale protuberances	Bedrock low drag (streamlined), positive relief landforms - sliding glacier sole		8
Meso-scale rock grooves	Carving of linear depressions in bedrock by warm-based, sliding glaciers	Bedrock linear incisions and rock basins (individual depressions carved in bedrock, often associated with *roches moutonnées*)		9, 10, 11 and Appendix S2.9
Meso-scale subglacial meltwater channels	High englacial hydraulic gradients	Bedrock channel incision (Glasser and Bennett, 2004), with undulating longitudinal profile (channel undulation index $\psi > 0$; Galofre et al., 2018)	*V-index* ≤ 0.1, ψ *index* > 0	12, 13
Tunnel valleys, large (10^3 m wide, 10^2 deep, 10^5 m long)	Erosion by channelized meltwater produced by ice sheets	Bedrock or glacigenic sediment incised with elongate, overdeepened depressions	*V-index* ≤ 0.1	14 and Appendix S2.10

3. Methods

3.1. Extant VFF and topographic contexts

Extant VFF were identified based on criteria specified by Milliken et al. (2003), Head et al. (2010), Souness et al. (2012) and Hubbard et al. (2014). The broad topographic contexts of VFF in Phlegra Montes were characterised using imaging and elevation data. This mapping also allowed the spatial distribution of extant VFF to be determined in topographic-geomorphological context. To be considered glacial, VFF must be characterised by: (1) features suggestive of viscous flow over or around obstacles, in response to changes in underlying slope; (2) contextual topography indicative of modification by viscous flow over or around obstacles; (3) surface texture and morphology distinct from summital areas, inter-valleys and peripheral terrain; (4) longitudinal foliation, consisting of narrow ridges and furrows, where VFF are affected by local flow constriction; (5) extensively lineated surfaces, where VFF are laterally confined (producing LVF), and; (6) moraine-like ridges (MLR) that bound or partition VFF surfaces displaying foliation and/or lineation associated with viscous flow. VFF exceeding 50 km^2 (VFF > 50; Appendix S1) were mapped as area features in a GIS, and then classified by type (LVF/LDA/COMP/CCF), with surface area also measured - e.g. LVF 393 refers to a LVF of 393 km^2.

3.2. Shallow radar identification of VFF subsurface reflectors, and determination of VFF bulk dielectric value, total thickness and ice purity

To determine the ice content, purity and total thickness (t) of GLF in Phlegra Montes, we analyzed SHARAD data along tracks crossing Phlegra Montes (Appendix S2.1). The bulk dielectric value of VFF is measured to constrain t and ice purity. SHARAD signals reflect at contrasts in the real part of the relative permittivity for various materials, e.g. between air and rock or ice and rock. Relative permittivity (dielectric constant) varies on Mars from 1 (atmosphere) to ~12 (dense basaltic lava flows). The dielectric value for most non-porous water ice on Mars ranges from ~3 to 3.2 (Plaut et al., 2007; Holt et al., 2008; Plaut et al., 2009; Grima et al., 2009), values greater than 3.2 generally implying some volume fraction of lithic material. Complementary assessments of VFF average thickness, based on surface area measures (after Karlsson et al., 2015) and surface lithic composition (after Baker and Carter, 2019), are provided in Appendix S2.2 and S2.3.

Radar profiles (radargrams) are interpreted in several steps, including clutter mitigation and depth correction. First, each radargram identified to have potential subsurface interfaces is compared with a simulated radargram, based on MOLA topographic data. Simulated radargrams use topographic facets to predict where reflections originating on the surface, both from nadir and to the side, will lie on the observation in time delay. Frequently, across-track surface reflections appear in greater delay than the nadir point (thus beneath the surface) due to their longer travel distance. These reflections, commonly called clutter, do not indicate a subsurface interface and are excluded from interpretation. Thus, where clutter is predicted and matches a potential subsurface interface, we do not interpret a subsurface reflection. On the other hand, when clutter is not predicted for a location, but a reflection appears, we interpret that to indicate a subsurface interface and record its position and time delay.

Once clutter echoes have been identified and excluded, the second step is to use surface topography and knowledge of the surrounding terrain to estimate a subsurface geometry associated with the reflection and derive a dielectric constant. In the case of LDA, this step requires an assumption that the surrounding terrain maintains its geometry in locations covered by the LDA (e.g. Holt et al., 2008; Plaut et al., 2009). To determine the bulk dielectric value of LDA 1694, we use an equation that relates distance to velocity and relative permittivity (Seu et al., 2007).

$$t = 2d\,\varepsilon'^{0.5}/c \quad (1)$$

where t is the two-way travel time, d is distance, ε' is dielectric constant and c is the propagation speed of electromagnetic waves through a vacuum. Having found the peak terrain elevation along each radar profile and measured the time delay to calculate the relative permittivity ε', we also performed a test to flatten the basal reflector to match the surrounding terrain. To do this, radargrams are "depth corrected" by moving all reflections that arrive after the nadir surface point towards the surface using the same equation as before. This method is less rigorous but offers a visual way of comparing dielectric values rather than focusing on time and thickness at a single point (Fig. 6).

3.3. Morphological analogues of erosional landforms produced by warm-based ice

Candidate morphological analogues of terrestrial landforms considered diagnostic of erosion by warm-based glacial ice were identified by reference to the geomorphological contexts in which the VFF occur and to the insights offered by Glasser and Bennett (2004); the location of candidate analogue landforms is shown in Appendix S2.4. The set of diagnostic landforms (Table 1) is supported by morphometric indexes that have been used to infer the genesis of valleys, valley-heads and channels. Bouquety et al. (2019) applied the valley index (*V-index*) to discriminate between glacial and fluvial valleys on Mars. *V-index* compares valley cross-sectional area (*Ax*) against an ideal V-shaped valley cross-section (*Av*) of the same height and width (Zimmer and Gabet, 2018). Ideal U-shaped (glaciated) valleys have a V-index >0 but ideal V-shaped (non-glaciated) valleys have a V-index <0 (Zimmer and Gabet, 2018). Bouquety et al. (2019) interpreted martian valleys with a *V-index* > 0.2 as glacial but <0.1 as fluvial; we place the fluvial threshold at ≤0.1. For Phlegra Montes, *V-index* was calculated from elevation data extracted from HRSC 50 m/pixel DEM and is defined as.

$$V - index = (Ax/Av) - 1 \quad (2)$$

Cross-sectional area was measured from the deepest point of each valley cross-section to the elevation of the lowest valley shoulder. This is equivalent to the full-valley cross-section measure of Zimmer and Gabet (2018), which had a predictive accuracy of 65% for glaciated valleys, 68% for non-glaciated; the truncated-valley measure of Zimmer and Gabet (2018) is slightly more predictively accurate (66% for glaciated valleys, 70% for non-glaciated) but is more subjective.

Bouquety et al. (2019) also applied morphometric criteria developed in the terrestrial context (Barr and Spagnolo, 2015; Evans and Cox, 2017) to identify glacial corries on Mars. Applying the method of Barr et al. (2019), the ratios of corrie width-to-height (*W:H*) and length-to-width (*L:W*) were measured for candidate corries in Phlegra Montes. *L* is the length of a line plotted from the mid-point along the corrie threshold (the crest of the convexity defining the corrie distal margin) to the mid-point along the corrie backwall crest. *W* was measured normal to the mid-point of L. *H* was measured as the elevation difference between the corrie floor (under the intersection point of the measurement lines of *W* and *L*) and the elevation of the backwall crest. For corries on Earth, Barr and Spagnolo (2015) reported mean morphometric ratios of $W{:}H = 2.72$ and $L{:}W = 1.03$. Bouquety et al. (2019) interpreted valley heads on Mars as glacial corries/cirques by reference to these morphometric criteria.

Galofre et al. (2018) applied an undulation index (ψ) to identify channels of subglacial genesis on Earth. To measure ψ, channel longitudinal profiles were plotted from elevation data extracted from a 2 m/pixel HiRISE DEM. ψ is defined as.

$$\psi = (h_{max} - h_{min})/\Delta H \quad (3)$$

where h_{min} and h_{max} are, respectively, the local minimum and maximum elevations along a channel reach with positive topographic gradient and ΔH is the total along-channel elevation change. Galofre et al. (2018) concluded that channels with $\psi > 0$ are unequivocally of subglacial genesis.

Glasser and Bennett (2004) classified landforms of warm-based glacial erosion on Earth at micro-scale (<1 m), meso-scale (1 m to 1 km) and macro-scale (>1 km). However, owing to constraints placed by relying mainly on CTX images, we limited the search to diagnostic meso-to-macro-scale landforms (Table 1). In deciding if the morphological evidence supports an interpretation of morphogenesis in a warm-based subglacial environment, the most conservative palaeoenvironmental interpretation should be assumed, consistent with the general viewpoint that regional warm-based glaciation on Amazonian Mars has been extremely rare. Therefore, strong morphological indicators must be observed to reject the most conservative interpretation in favour of the alternative of warm-based glaciation. In that respect, ψ and the morphometric indexes offer important discriminant metrics.

4. Results

4.1. VFF in Phlegra Montes and associated macro-scale landforms

4.1.1. Distribution, topographic contexts and forms

VFF > 50 occur in Phlegra Montes from ~32° - 41° N (Fig. 1; Appendix S1) and have a total surface area of ~16,600 km^2. The VFF have four main topographic contexts. (1) VFF occur in the intra-montane basins of massifs, on the flanks of isolated mountains or small massifs and in long, WNW-ESE trending grabens (Fig. 2a). VFF are not widely present in summital areas (Fig. 1; see also Appendix S2.4). Intra-montane basins occupied by these VFF include both flow linkage and outlet to lower levels through short, interconnecting passes, and through longer troughs. VFF in these settings, partially filling topographically constrained elongated negative relief, were mapped as LVF. (2) Lobate piedmont aprons with viscous-appearing surface forms were mapped as LDA. They occur around the flanks of the northern spine of Phlegra Montes and on piedmonts surrounding isolated mountains or small massifs (Fig. 2b). (3) Some massifs or more compact uplands are fringed by LDA fed from the uplands through linear corridors by LVF; these compound VFF were mapped as COMP (Appendix S1). (4) Some craters, both upland and lowland, are partially occupied by viscous, concentrically ridged material, mapped as concentric crater fill (CCF; Fig. 2b).

4.1.2. Sharad observations - LDA 1694 subsurface reflector and thickness

A regional survey of available SHARAD data found seven relevant radargrams not adversely affected by topographically induced radar clutter (Appendix S2.1). These all cross over or near to LDA 1694 (Fig. 2b) and exhibit a strong subsurface reflection (Fig. 3). For the observations with detections under LDA 1694, we assume a flat basal geometry that extends from the surrounding, approximately flat terrain towards the west and south. Fig. 3 shows that the foreland of LDA 1694 is a nearly flat surface at ~ − 3300 m, and that the highest point of the LDA along a SHARAD orbital ground track (not at the contact with the abutting massif but slightly offset) is at −2802 m, for a maximum potential thickness of ~500 m (Table 2). Applying the time delay (Section 3.2) yields an average relative permittivity (ε') of 3.21 ± 0.11 (Table 2; range 3.07–3.36). This value is consistent with >96% pure water ice (Bramson et al., 2015). Applying a depth correction (Section 3.2), we find that a value of ε' = 3.15, consistent with pure water ice, does not provide a perfect match with the surrounding terrain, but a value of ε' = 3.6 does a better job. This value is consistent with an ice purity of 88–90% by volume or a stratified deposit of pure ice (ε' = 3.15) overlain by regolith. Two possible end members are 396 m of ice overlain by 4 m of high-density regolith (ε' = 8.0) or 390 m of ice overlain by 10 m of low-density regolith (ε' = 5.0). Complementary morphometric and flow-based estimates (Appendix S2.2) indicate that average VFF > 50 thickness in the region ranges from <100 m to 200 m (LDA 1694 having the largest average thickness).

4.1.3. LDA 1694 bulk dielectric properties, ice purity and surface variation

The dielectric value of LDA 1694 is 3.2–3.6, higher than the nominal value of water ice (3.15) and higher than the LDA studied by Holt et al. (2008), Plaut et al. (2009) and Petersen et al. (2018). A dielectric value of 3.6 is consistent with a 396 m thick glacier with ~4 m of a dense, rocky material lag on top. If so, the bulk of the LDA must be pure ice and the lag must be too thin for SHARAD to detect it (i.e. <15 m). However, another possibility is that the dielectric value represents a homogeneous mixture of ice and up to ~10% dust. This interpretation would be consistent with LDA in other parts of Mars. Further insights to the clastic surface properties of LDA 1694 are provided in Appendix S2.3. Finally, if the ground under LDA 1694 were not flat but, instead, glacio-

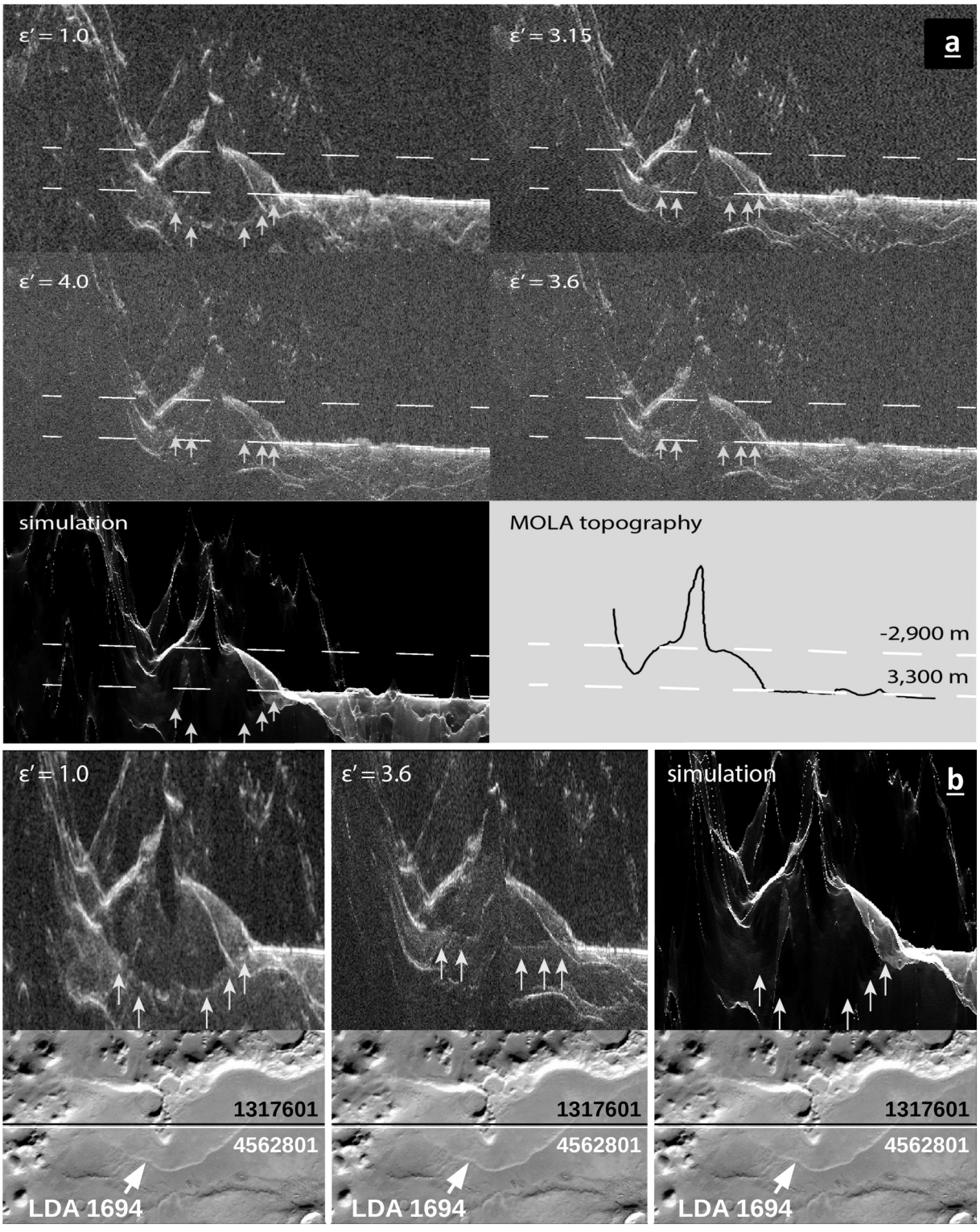

Fig. 3. (Panel a) Section of SHARAD profile 4,562,801 crossing LDA 1694 showing time delay (ε' = 1.0); depth corrections based on ε' = 3.15, 3.6, and 4.0; a simulation based on MOLA topography; and MOLA topography at the nadir point. Elevations of −2900 and − 3300 are identified by the dashed lines. The basal reflection with ε' = 3.6 most closely matches the surrounding terrain. Constant elevations are not horizontal because the radargrams and simulation are based on a 3396/3376-km ellipsoid datum, which makes level topography look inclined locally. (Panel b) Section of SHARAD profile 1,317,601 crossing LDA 1694 (black line, lowermost panels) showing time delay (ε' = 1.0), depth correction with ε' = 3.6; and a simulation (white line is SHARAD profile 4,562,801).

isostatically depressed, the dielectric could represent a glacier of pure ice (ε' of 3.15). However, there is no evidence of crustal flexure beneath or immediately surrounding the LDA at this location or for LDA at other sites around Mars.

4.2. *Candidate landforms interpreted as indicators of warm based erosion*

In this section we present the results of a search for examples of candidate analogues of the terrestrial landforms considered diagnostic

Table 2
Estimates of maximum potential thickness of LDA 1694. Fig. 3 shows the terrain surrounding LDA 1694 to be nearly flat ~ −3300 m, with the highest point of the LDA along a SHARAD orbital ground track at −2802 m, giving a maximum potential thickness of ~500 m.

Observation #	Two way time (μs)	Basal elevation (m)	Max elevation (m)	Max thickness (m)	ε'
13,17,601	2.381	−3300	−2900	400	3.19
31,29,401	2.917	−3300	−2802	498	3.09
36,60,801	2.943	−3314	−2810	504	3.07
45,62,801	2.334	−3302	−2914	388	3.26
45,98,402	2.578	−3292	−2864	428	3.27
46,55,101	2.381	−3300	−2910	390	3.36

of erosion by warm-based glacial ice (Table 1). Following the description of each analogue example, an interpretative justification of their candidate status as evidence of warm-based erosion processes is provided. The candidate landforms all occur within contextual landscapes characterised by the presence of VFF, from the criteria of Milliken et al. (2003), Souness et al. (2012) and Hubbard et al. (2014). Although the interpretations that follow cannot be definitive, being based only on remote sensing, we believe they are morphologically consilient with diagnostic terrestrial analogues and reasonable in their landscape context. We do not attempt to order the landforms by any implied significance; it is important that each landform is viewed as part of an integrated landscape system. Hence, the landforms are dealt with in the order presented by Glasser and Bennett (2004), which also corresponds broadly to their prevalence in Phlegra Montes (Appendix S2.4 shows

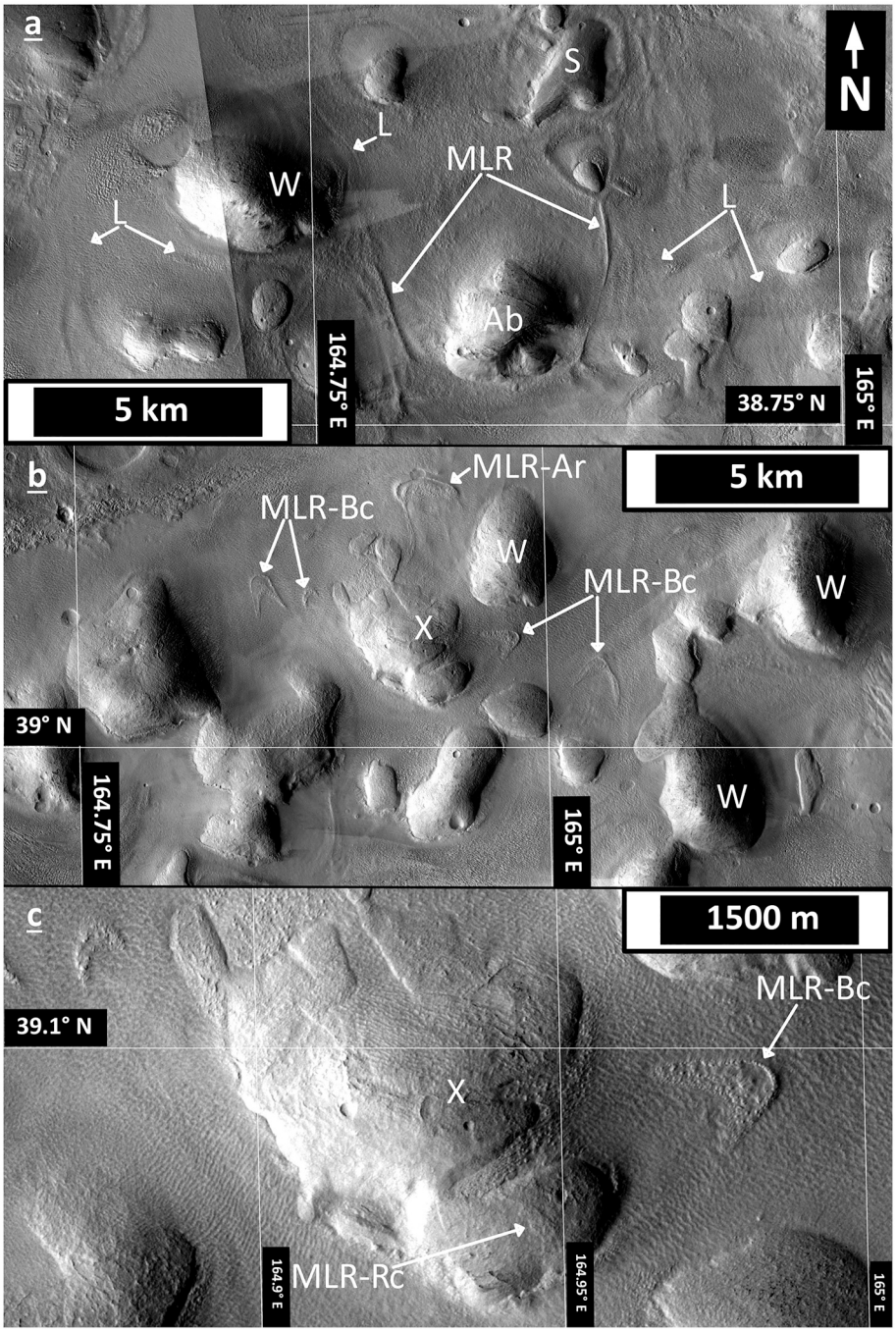

Fig. 4. (Panel a) Moraine-like ridges (MLR) in low terrain between smoothed, rounded topographic highs; labelled examples of whalebacks (W), abraded hills (Ab) and smoothed platforms (S). MLR orientations and junctions complement LVF flow lineations (L). CTX image mosaic: D15_033239_2214_XI_41N195W; B19_017165_2213_XN_41N195W. (Panel b) Arcuate ridges (MLR-Ar) and barchanoid ridges (MLR-Bc) also occur, overlooked by smoothed, whaleback (W) hills. Hill X located for reference with panel c. CTX image D15_033239_2214_XI_41N195W. (Panel c) Band resembling a recessional moraine (MLR-Rc) lies orthogonally across the smoothed, whaleback prominence at the southern end of hill X. The downflow pointing curvature of the MLR-Rc and the MLR-Bc are mutually consistent and congruent with small, streamlined forms in the lee-side indentation into hill X and lineations between hill X and the MLR-Bc. CTX image B19_017165_2213_XN_41N195W. CTX image credits: NASA/JPL/MSSS.

locations of candidate landforms. Appendix S3 is a Google Earth [Mars] kmz file, providing the areo-referenced locations of the landform candidates).

4.2.1. Areal scour

Fig. 4a-c show a landscape of smoothed, often elongated hills separated by viscous flow components of the LVF 4258 complex (Fig. 1 and Appendix S1). Several of these elongated, smoothed hills narrow to a rounded summital ridge and some are traversed by subtle bands orthogonal to the long axis of the hill (e.g. Fig. 4b,c). The long axis orientation of these hills is complemented by branching, arcuate or chevron-shaped ridges within the LVF. The branching ridges compartment basins in the low terrain between elongated hills and smoothed platforms (e.g. Fig. 4a). The orientations and junctions of branching ridges are complemented by viscous flow lineations on the adjacent LVF surface (Fig. 4b).

4.2.1.1. Interpretation. In this landscape, the narrow, branching LVF ridges are contextual and morphological analogues of lateral and medial moraines (Fig. 4a, labelled MLR). In context, the arcuate and chevron-shaped ridges are strikingly like arcuate moraines and barchanoid moraines (Fig. 4b,c, respectively labelled MLR-Ar and MLR-Bc). Elongated hills with narrow, rounded longitudinal ridges are morphological analogues of whalebacks, streamlined landforms resulting from subglacial scour. Bands draped orthogonally across the long axis of streamlined hills and rock platforms are consistent with being recessional moraines (MLR-Rc), deposited by thicker ice that formerly covered the platforms (Fig. 4b-c). In the context of LVF flow direction indicators (topography, general slope, surface lineations), MLR-Bc point apex-downflow (their arms extending up-flow). These characteristics are consistent with the interpretation of MLR-Bc as morphological and palaeoflow analogues of terrestrial barchanoid moraines, which form when pre-existing glacial sediments are overridden during late stage warm based glaciation (Golledge and Stoker, 2006). The presence of viscous material bounded by a pitted margin beyond the MLR-Bc suggest a similar sequence of events, involving small, localized overriding flows across a pre-existing ice-rich substrate. The downflow pointing curvature of the MLR-Rc and the MLR-Bc are mutually consistent, and congruent with small, streamlined forms in the lee-side indentation into hill X and lineations between hill X and the MLR-Bc (Fig. 4c).

Overall, in the context of Fig. 4a-c, the textures of the eroded surfaces and smoothed forms, and the form of the whaleback hills and MLR, are consistent with streamlining glacial scour across a considerable area. An important implication arising from this landscape interpretation is that these forms have become exposed due to significant LVF thinning (or, possibly, increasingly deep dissection of troughs and basins between

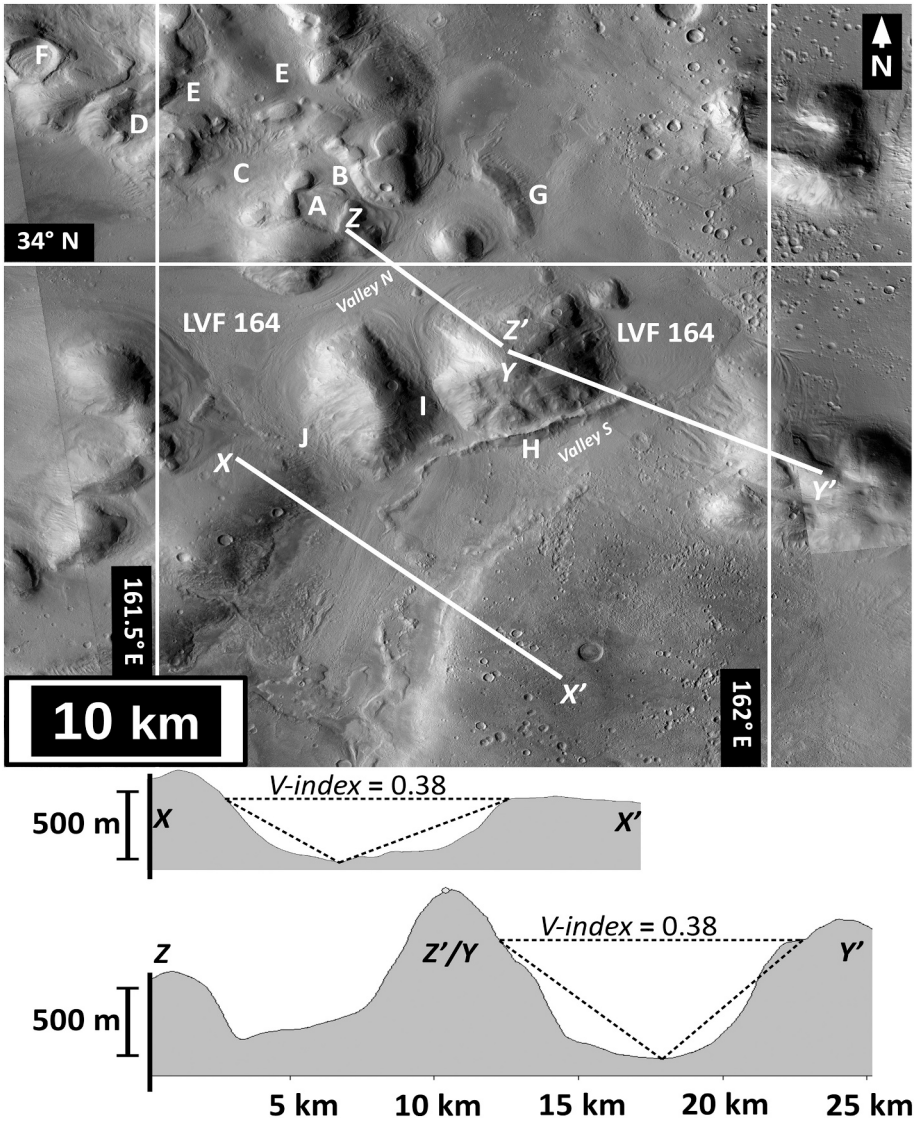

Fig. 5. Scene part of CTX image (P22_009794_2155_XI_35N198W), showing landscape surrounding trough (valley N) occupied by part of LVF 164. (A) LVF occupying open upland basin. (B) LVF occupying upland trough, separated from A by ridges. (C and D) unoccupied open upland basins. (E) troughs breaching backwall of C and D. (F) Open upland basin (breached impact crater) occupied by lineated fill. (G) transverse ridge, partially blocking valley N. (H) ridge extending along edge of valley S, beyond terminus of LVF 164. (I and J) outlets of LVF 164. Lines *Z*-Z', Y-Y′ and X-X' are cross-sectional profile paths. X-X' and Y-Y′ are not significantly affected by a LVF and each has a *V-index* > 0.2, consistent with glacial incision. Elevation data: HRSC (data credit ESA/DLR/FU Berlin). CTX image credit: NASA/JPL/MSSS.

increasingly exposed intervening highs). A competing, overarching interpretation is that the smoothed forms and ridges are aeolian in origin, but this would ignore the directional variability of these forms, particularly the apex directions of the MLR-Bc, and the close relationship between the configuration of those forms and the LVF flow indicators. Local katabatic winds would not provide a good explanation either, as most MLR-Bc are located downflow of prominences rather than being in valleys.

4.2.2. Glacial troughs

LVF 164 (Fig. 5) occupies valley N, a feature not sharing the same alignment as the major fault-valleys hosting VFF in Phlegra Montes (e.g. Fig. 2a). The valley possibly has a catenary cross-section, but the full cross-sectional form is obscured by the LVF (profile *Z*-Z', Fig. 5). Basin A is a perched, breached depression, occupied by a viscous fill. Trough B, separated from basin A by ridges, is occupied by a viscous fill, and is confluent with LVF 164 in valley N. Basins C and D are unfilled. The backwalls of both C and D are breached by troughs E incised into the summit of the massif. Basin F is a breached crater, partially occupied by a lineated fill. The mouth of valley N is partially enclosed by rock ridge G, beyond which the LVF recurves and terminates at the entrance to the parallel valley S, crossed by profile Y-Y′; valley S has a catenary cross-section (*V-index* 0.38) and does not appear to have a significant fill. Valley S descends south-westward, enclosed by ridge H, which has a maximum relative height of ~175 m. West of ridge H, cross-section X-X' has a catenary profile but is partially occupied by a transfluent LVF that exits valley N through pass I (similarly, LVF-occupied pass J links valleys N and S). Long valleys, other than *E*-W grabens, are rare in Phlegra Montes. However, short, LVF-occupied passes between mountains are very common. In Fig. 6a a LVF pinches-out in a pass between two mountains and the lee-side slope, beyond the pass, is incised by channels. The pass in Fig. 6b is smooth textured, intervenes between rounded, subtly lineated hilltops and overlooks basins occupied by LVF. Both passes have catenary cross-sections: profile W-W′, *V-index* 0.31; profile V-V′, *V-index* 0.28.

4.2.2.1. Interpretation. The *V-index* of valley S (cross-section Y-Y′, Fig. 5) is consistent with it being a glacial trough (cf. Bouquety et al., 2019). The *V-index*, and landform contexts, of the passes in Fig. 6 (cross-sections W-W′ and V-V′) are consistent with them being transfluent glacial cols (terrestrial analogues of which often attain catenary form; e.g. Hambrey, 1994). Both Y-Y′ (Fig. 5) and W-W′ (Fig. 6a) retain minimal fill but this is typical of terrestrial glacial analogues determined to be catenary. Cross-section profiles *Z*-Z' and X-X' (Fig. 5) also most likely represent glacial catenaries but with more significant viscous fills. The shallow catenary form of trough Y-Y′ (Fig. 5) is typical of glacial troughs in several settings on Earth, most notably in Patagonia and Antarctica (Hirano and Aniya, 1988). In context, the valley forms in Fig. 5 are consistent with the effects of warm-based glacial erosion. The LVF-occupied summital basin A and trough B, and trough complex E, indicate that the massif north of valley N is glaciated – and was formerly more extensively glaciated. Ridge H (Fig. 5) is interpreted as a MLR, deposited between the main south-westward flowing glacier in valley S and outlet glaciers descending from valley N through transfluent cols (e.g. pass I). Hence, ridge H is indicative of previously more extensive valley glaciation, the ridge height indicating former glacial thickness of ~175 m (H appears to have been overridden, and smoothed, by a late-stage outflow through transfluent col. I, presumably permitted by the withdrawal of the main glacier snout east of H in valley S). The

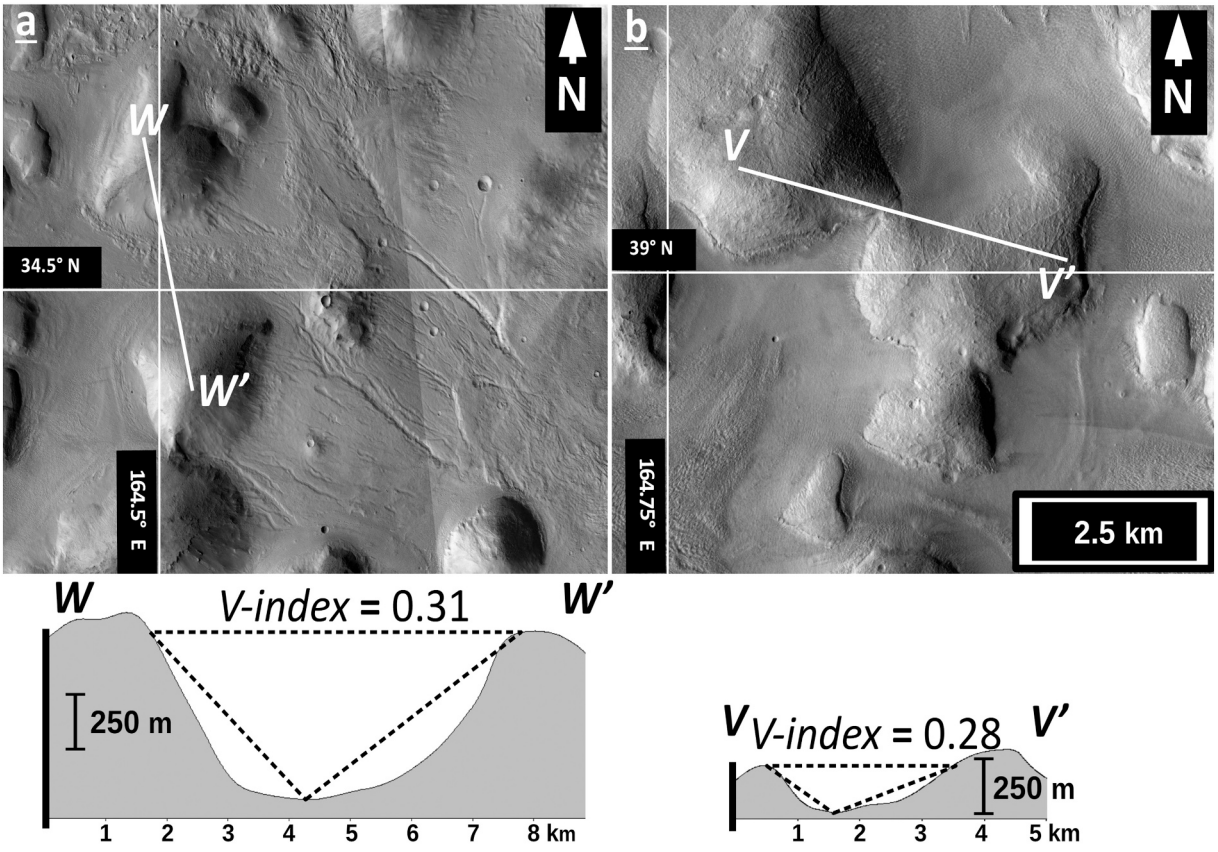

Fig. 6. (Panel a) LVF pinching-out in catenary pass between mountains. Pass cross-section W-W′ is catenary (*V-index* 0.31) Note channel incision east of pass W-W′. (Panel b) Pass V-V′ is unoccupied and catenary in form (*V-index* 0.28) but overlooks basins occupied by LVF. Both W-W′ and V-V′ are characteristic of glacial erosion (*V-index* > 0.2). Panel a from CTX image P16_007368_2152_XN_35N195W. Panel b from CTX image cirB19_017165_2213_XN_41N195W. Elevation data: HRSC (data credit ESA/DLR/FU Berlin). CTX image credit: NASA/JPL/MSSS.

transfluent cols in Fig. 6 also are indicative of former thicker glaciation. The lee-side channels beyond the col. in Fig. 6a possibly are indicative of glacial meltwater discharges by ice at the col. or, formerly, beyond it. A competing interpretation of the trough and col. landscapes is that these forms are glacially occupied grabens, with minimal modification by glacial erosion. However, to be convincing, this interpretation would have to include all candidate cols with catenary cross-sections – and this would imply faulting of very high spatial-density and variability in strike. Instead, it is more likely that the troughs and cols represent erosion by glaciers that flowed through pre-existing valleys (including grabens, e.g. Fig. 2a), and became sufficiently thick to exploit saddles between neighbouring mountaintops. Judging the relative robustness of the competing interpretations depends on how the within-trough and col-adjacent forms are interpreted and, hence, will be revisited.

4.2.3. *Corries*

In Fig. 7 a small, perched basin A is occupied by a viscous fill, which is confluent with the small LVF occupying trough B (which descends to LVF 164; Fig. 5 shows wider context). In the same massif as A and B, the open, amphitheatre-shaped basins C and D (Fig. 5, Fig. 7) have length-to-width ratios of 0.93 (C) and 0.85 (D) and width-to-height ratios of 3.55 (C) and 2.78 (D). Maximum backwall slopes are ~19° (C) and ~ 21° (D). Both basins are fronted by a slight convex-up lip. The sloping forelands beyond these lips are incised by parallel sets of lineations. The backwall of basin C is breached by the LVF-occupied trough B; both C and D are also breached by unfilled troughs (E). Basin F is a breached

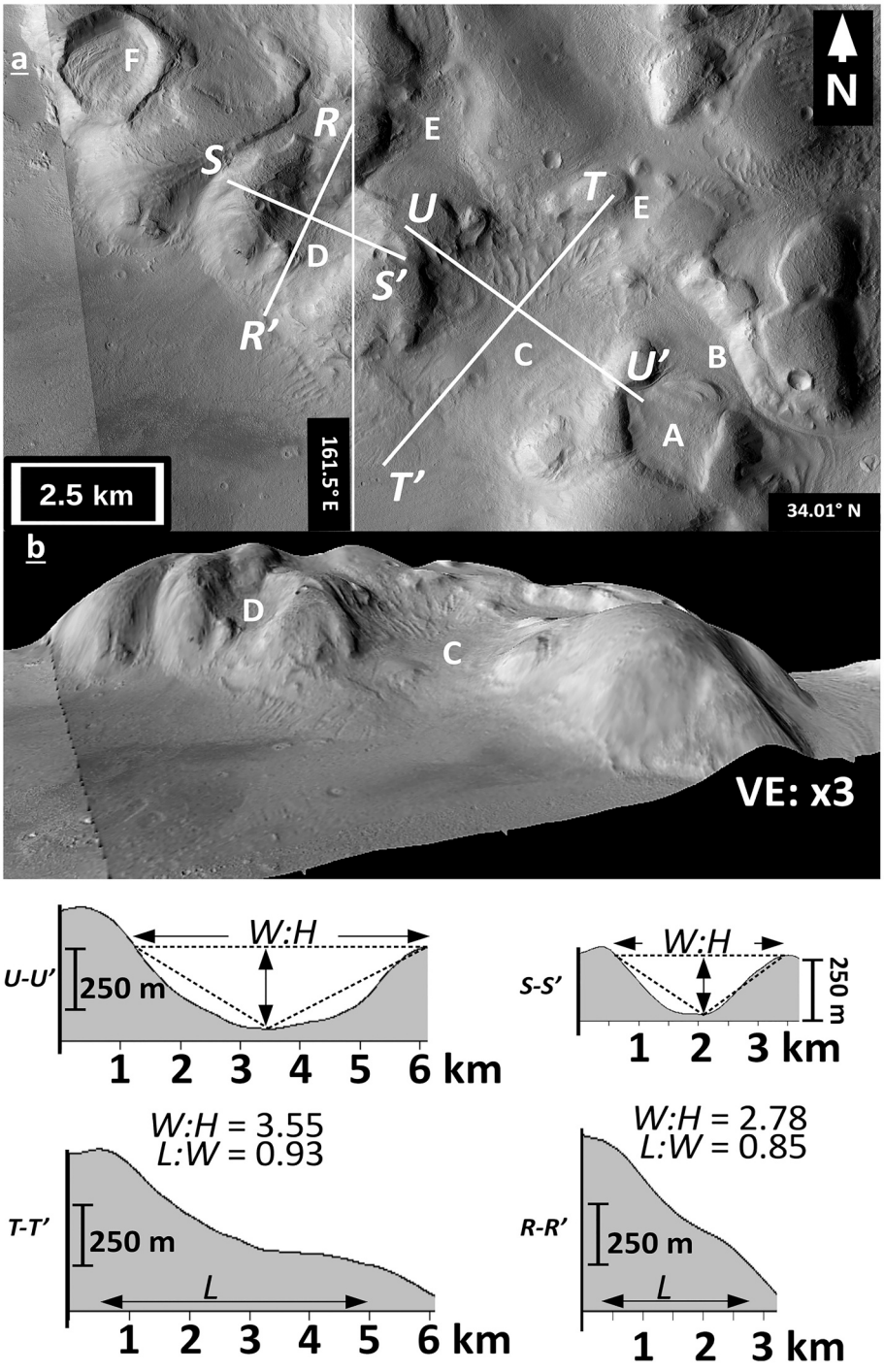

Fig. 7. (Panel a) Compact massif incised by perched troughs and open (amphitheatre-shaped) basins. (A) perched basin occupied by a viscous fill. (B) perched trough occupied by small LVF (descends to LVF 164; wider context in Fig. 5). (C, D) Amphitheatre-shaped basins. (E) Unfilled summital troughs. (F) Breached impact crater, occupied by lineated basin fill. (Panel b) Basins C and D have a form consistent with being glacial corries: *V-index* 0.33 (C) and 0.19 (D); length-to-width ratio 0.93 (C) and 0.85 (D); width-to-height ratio 3.55 (C) and 2.78 (D); maximum backwall slopes are ~19° (C) and ~ 21° (D). Both C and D are fronted by a slight convex-up lip, also characteristics of glacial corries. Although the morphometric characteristics of C and D are consistent with glacial corries, they should also be considered in the context of crater truncation without glacial overdeepening (see Appendix S2.6). From CTX image P22_009794_2155_XI_35N198W. Elevation data: HRSC (data credit ESA/DLR/FU Berlin). CTX image credit: NASA/JPL/MSSS.

impact crater, occupied by a lineated fill.

4.2.3.1. Interpretation. The cross-sectional and longitudinal characteristics of basins C and D (*L:W* and W:H, Fig. 7) are consilient with terrestrial corrie analogues, and with forms interpreted as corries/cirques on Mars (Bouquety et al., 2019). These basins fit within a continuum of erosional glacial valley forms of varying length, ranging from cols to troughs (cf. Aniya and Welch, 1981). Additionally, the longitudinal profile of basins C and D, including the development of a slight frontal lip, is morphologically consistent with enhanced flow resulting from transference of water to the glacier base in crevasse zones (Alley et al., 2019) and, in thinner ice, erosion by rotational basal sliding (Lewis, 1949). Although the lip is less developed in C and D than in analogues described by Bouquety et al. (2019), it is typical of many terrestrial corries (examples in Appendix S2.5). The presence of parallel lineations beyond these lips is consistent with subglacial abrasion having occurred beyond the candidate corries, providing further evidence of formerly more extensive glaciation. Morphologically, basin A containing the viscous fill is similar to basins C and D, with a similar *W:L* of 0.97, suggesting it could be a glacially-occupied corrie. However, the equidimensional axial form of corries (Barr and Spagnolo, 2015) is closely matched by the cross-sectional form of impact craters, which tend to be circular in planimetric form and parabolic in section. On Earth, Pleistocene corries developed at the head of pre-existing valleys formed in earlier tectonic and fluvial contexts. In the Mars context, it is likely (even probable) that most candidate corries, in the sense of being

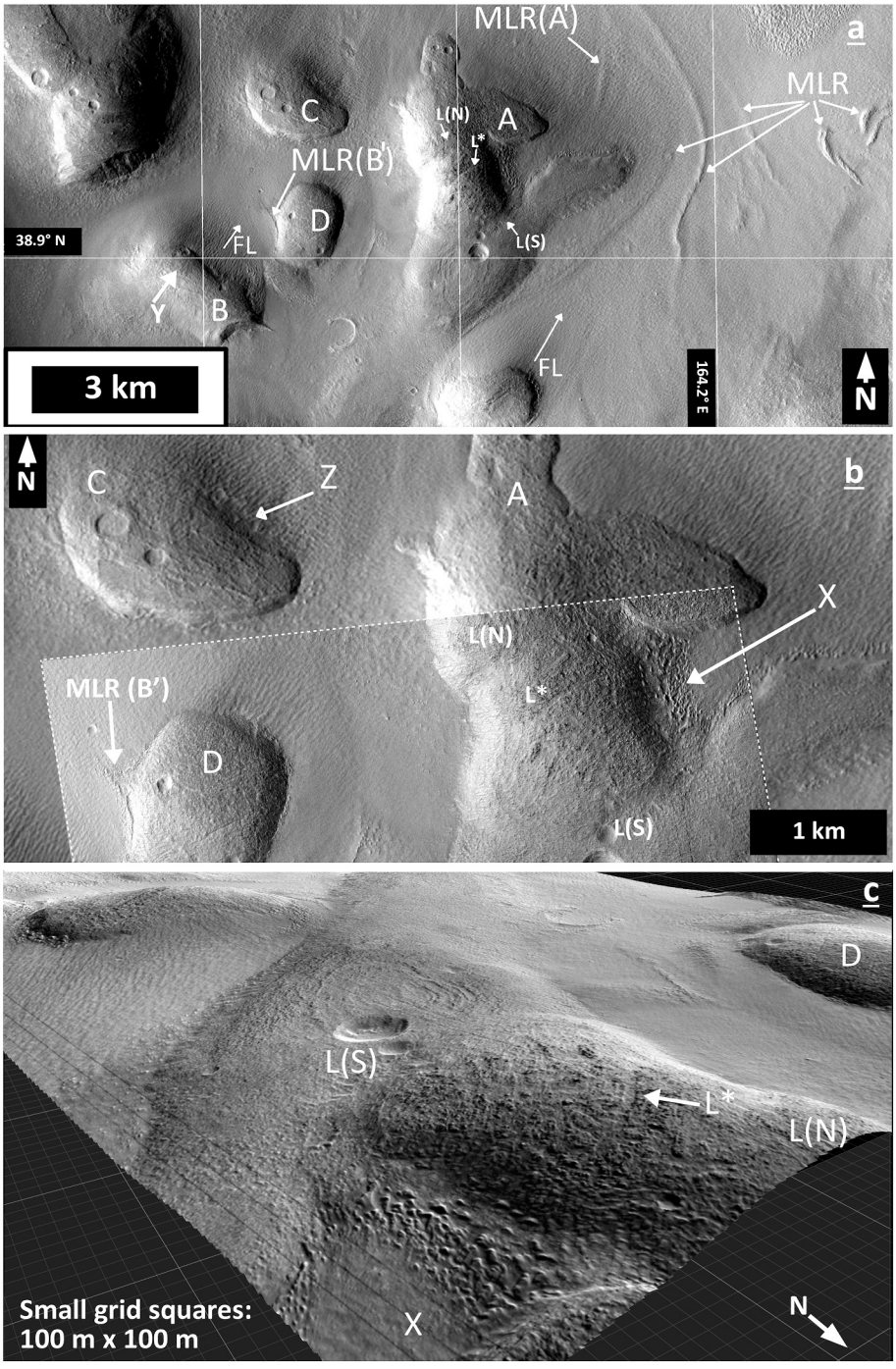

Fig. 8. (Panel a) Smooth bedrock platforms (examples labelled A, B, C, D). LVF characterised by prominent MLR and flow lineations (FL). Note parallel lineations on platform A (circled, between arrows L) and rimless craters on the platforms. Contextualized by flow lineations, indentations on northeast side of platforms A, B and C are lee-side basins (indentation Y into B is less developed than indentation into A). North-eastward movement of ice and debris, from platform B basin indicated by MLR (B′) on platform D. MLR(A') extends northeast from platform A basin and converges with main MLR assemblage (arrowed). (Panel b) CTX image with HiRISE insert (within white dotted border) showing details of lee-side basins (arrowed X and Z) on platforms A and C, and MLR B′ marginally onlapping platform D. Platform A is textured by generally SW-NE lineations between L(N) and L(S); lineation L* is especially clear. (Panel c) HiRISE 1 m DEM showing topographic context of platform A and the lineations texturing its surface between L(N) and L(S); L* (arrowed) is an incised feature. CTX image G20_026158_2190_XN_39N195W. DEM: HRSC (data credit ESA/DLR/FU Berlin). Image credits: NASA/JPL/MSSS. HiRISE image: ESP_062909_2190. HiRISE DEM: from stearo pair ESP_062474_2190_E SP_062909_2190. HiRISE credits: NASA/JPL/U of A. HiRISE DEM produced on *AreoBrowser* (https://areobrowser.com/#/id=ESP_062909_2190).

overdeepened glacial basins, developed from pre-existing impact craters (e.g. open basin F, Fig. 7). In the substrate-context of Phlegra Montes, impact craters with no fill tend to have very V-shaped cross-sections, but craters with fill are U-shaped to rectangular in cross-section (examples in Appendix S2.6). Therefore, it is possible that the characteristic morphometric properties of corries are also integral properties of filled impact craters, even those with no outlet that could not have been overdeepened. Consequently, the morphological evolution of the open upland basins C and D in Fig. 7 can be only tentatively ascribed to glacial erosion solely based on their morphometric affinity to corries. The general context of these forms, however, suggests that interpreting them as corries is not unreasonable.

4.2.4. Lee-side rock basins/cavities and streamlined forms

In Fig. 8a, smooth platforms (e.g. A, B, C, D) lack viscous flow features. Craters on the platforms are rimless. The LVF, characterised by prominent MLR and flow lineations (FL), are constrained and directionally guided by the platforms. However, the platforms are textured by parallel, shallow grooves and lineations (e.g. L* on platform A, Fig. 8a,b, c), and are onlapped by ridges (e.g. MLR(B′) on platform D, Fig. 8a, b, c). The northeast side of platforms A, B and C are indented (features X, Y, Z), the indentation into platform A being especially pronounced (Fig. 8a, b, c feature X). Lineation orientations on platform A are coherent with MLR and flow lineations on adjacent LVF surfaces and platform D. Directional statistics presented in Appendix S2.8a show that lineation orientations sampled from platform A are directionally consistent with MLR and flow lineations on surrounding LVF surfaces.

4.2.4.1. Interpretation. Lacking viscous flow features, the platforms in Fig. 8a are inferred to be rock. The onlapping MLR and shallow grooves/lineations suggest that the platforms have formerly been overridden and linearly incised. This interpretation is supported by the statistical coherence between the orientation of lineations on platform A and flow indicators (MLR and flow lineations) on surrounding LVF surfaces (Appendix S2.8a). Rimless craters on the platforms are consistent with this interpretation, suggesting areal scour occurred with linear abrasion. Given the palaeoflow context indicated by the pattern of platform grooving and complementary MLR, indentations on the northeast side of platforms A, B and C are lee-side features (Fig. 8b and c). The indentation into platform A is a well-developed lee-side basin, open to the northeast, while the indentations into platforms B and C are less developed lee-side cavities - possibly incipient basins. North-eastward movement of ice and debris, from the lee-side cavity in platform B, is indicated by MLR(B′) on platform (D). MLR(A'), extending from the platform A basin, and converging with the main assemblage of MLR (arrowed), is likewise indicative of northeasterly debris transport. Hence, the basins and cavities appear to represent lee-side entrainment and erosion of platform material by overriding palaeoflows.

In context, the morphologies of the smooth rock platforms (including rimless craters) are consistent with scour by sliding ice. The smooth, rounded surfaces of the platforms, with zones of deeper linear incision, are consistent with streamlining scour with localized abrasion. The lee-side locations of the basins and cavities are consistent with plucking, where overriding ice lost close contact with its bed on the lee-side of protuberances. Formation of lee-side basins by plucking to the degree evident in on Platform A (Fig. 8a) is consistent with "quarrying", the process in which large bedrock blocks are eroded and entrained under sliding glaciers (Hallet, 1996). An overarching implication of plucking that has evolved to quarrying is that LVF thickness was formerly greater than at present, implying that quarry-like basins were originally subglacial lee-side cavities. An alternative interpretation is that they formed by backwasting through basin headwall plucking, without glacial overriding of the platforms. Both interpretations involve subglacial meltwater, but their implications differ with respect to former LVF thickness. Given the closeness of the form-flow relationships in this landscape, non-glacial erosion alternatives are hard to envisage but could include aeolian erosion and aspect-influenced surface degradation through loss of volatiles. Further examples of lee-side modification, ranging from steepening, without excavation, to cavity development associated with parallel grooves incised on lee-side slopes are provided in Appendix S2.7 and S2.8.

4.2.5. Meso-scale rock grooves

Parallel sets of grooves are a notable component of the landscape of Phlegra Montes across a variety of landscape scales. In Fig. 9, the surface of a platform ~1.5 km in down-valley extent (partly obstructing LVF 164) is textured by pits, 80–250 m wide (Fig. 5 provides context, label G). These coalesce towards the northeast into broad grooves, typically 150–200 m wide, 300–350 m long, separated by narrow inter-grooves. The pit-grooves parallel the local southwest to northeast flow lineations on LVF 164.

At a larger landscape scale, the northwestward sloping rock ramp in Fig. 10 (labelled A) extends downslope for ~6 km. This ramp is smoothed, lacking positive relief forms, but scored by long, narrow grooves (B). Simple, first order, confluences give the grooves the appearance of a channel-like network. The adjacent dome-shaped rock platform C also is smoothed but deeply incised by troughs D and E, which span dome C. Trough F, bisecting A and C, joins the trough occupied by LVF 393, at a hanging valley junction. The interface between trough F and ramp A comprises a subtle depression that converges into the head of the southernmost channel-like groove (at X in Fig. 10).

The grooves in Fig. 9 and Fig. 10 are microcosms of the extensive sets of parallel grooves incised into the rounded, dome-like mountains summits in Fig. 11a,b. Notably, these summit-crossing grooves are not arranged radially with respect to the mountain domes but, rather, produce a landscape with a "raked" appearance (Fig. 11a, arrows labelled C). Craters on mountain summits are rimless. Grooves become convergent only where the relief of the terrain is centripetal, i.e. where slopes become focussed radially inward to a common point (Fig. 11a, arrows labelled D). Where convergent macro-scale grooves occur, they develop sinuosity downslope, becoming channel-like in both form and network pattern (Fig. 11a,b). However, where terrain is not centripetally focussed, grooves are parallel and continuous for several kilometres, ascending and descending the smoothed, rounded mountains with no topographically induced deviation in alignment.

4.2.5.1. Interpretation. The grooves in Fig. 9 appear to have developed from individual "chiselled" pits that extended into longer, rough-textured pit-grooves or shallow, elongated basins. The pit-groove alignment, and their elongation parallel to the LVF lineations, suggest that they too record LVF movement towards the northeast. The development of grooves from pits on the cross-valley ramp is consistent with an erosional environment transitional between plucking and linear abrasion. Moreover, referring to platform A in Fig. 8, the assemblage of lineations there suggest a close relationship between linear abrasion and areal scour, leading to streamlined rock forms locally textured by shallow, parallel grooves. In this process continuum, subglacial protrusions become more deeply grooved and abraded over time as an accommodation governed by feedbacks between substrate topography, ice pressure and the through-put of basal debris from cavities to grooves. In Fig. 9, the distal narrowing of the grooves, beyond the foot of the ramp, is consistent with a diminishing flux of fluid and debris, as more uniform contact with the substrate was also re-established. In this setting, the development of pits and grooves is likely to reflect wet based subglacial conditions, at least as a local consequence of increased strain heating in the vicinity of the cross-valley ramp, which would have been a significant flow obstruction (Appendix S2.9 shows a historically significant terrestrial glacial analogue). Given the form of the platform in Fig. 9, and the parallel arrangement of the pits and grooves on its surface, aeolian erosion could be considered an alternative to the glacial

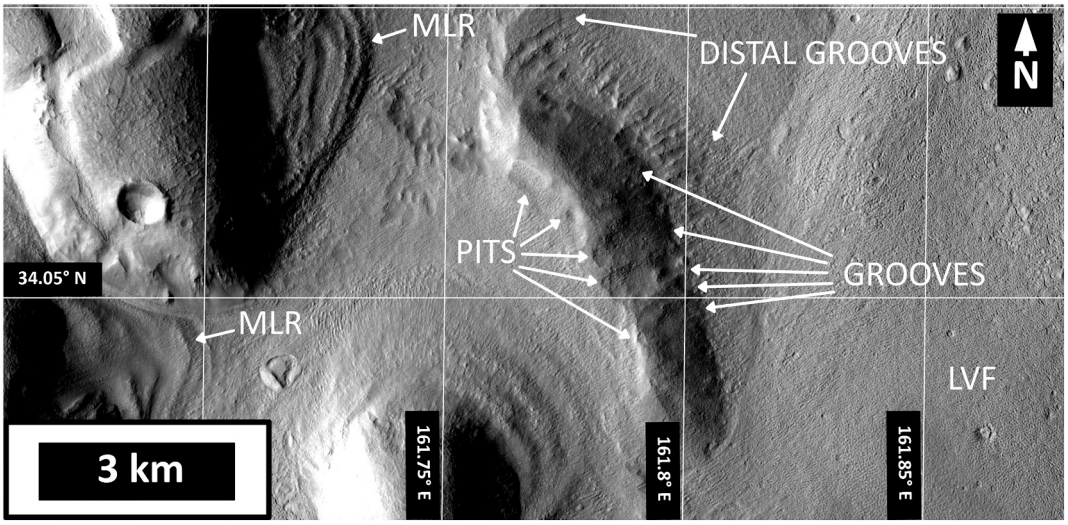

Fig. 9. Platform transverse to LVF 164 flow. The platform is convex-up, with an adverse stoss face sloping gently into the LVF flow and a lee face sloping more steeply to the down-flow to the northeast. The stoss face is indented by pits but the lee face is incised by longitudinal (i.e. LVF flow-parallel) grooves. CTX image G20_026158_2190_XN_39N195W. Image credits: NASA/JPL/MSSS.

hypothesis. This would ignore the consistency between the directionality of the platform grooves in Fig. 9 and the LVF flow indicators but would not fail as a hypothesis for that reason. Implicitly, however, this interpretation would also require non-glacial processes to have driven the morphological evolution of the LVF-occupied trough. While this could be envisaged at a single locality, the general consistency between form and indications of LVF flow suggest that glacial erosion is the more likely explanation on a valley-scale.

In Fig. 10, MLR G in troughs D and E suggest that the troughs in this larger landscape context were incised by transfluent glaciers that had expanded into trough F. In this context, it is possible that the channel-like grooves B were abraded by wet, sediment-rich, slurries at the base of a locally westward flowing, diffluent ice lobe that likewise expanded out of trough F, down-wearing the trough-ramp interface (at X, Fig. 10) in the process. Ice appears also to have flowed divergently through trough F, the point of divergence along the trough, between northward and southward flow (approximately at F, Fig. 10). Glacial transfluence (via eroded valley-head breaches) and diffluence (via valley-side overspill) represent a situation in which accumulation of ice (e.g. in trough F) exceeds its drainage (i.e. out of trough F), as a consequence of increased accumulation or diminished outflow (e.g. due to thickening of LVF 393). In the case of trough F, ice sufficiently thickened to have risen above the walls of the trough would have flowed to lower elevation across A and C. This scenario, predicated on the former greater thickness of LVF 393, could also explain the depth of incision of the trough hosting LVF 393. Non-glacial explanations for the landscape in Fig. 10 are hard to envisage, particularly given that the grooves (B) incised into platform A traverse a convex-up surface (from X). This makes mass wasting or subaerial fluvial erosion unlikely explanations.

At the largest landscape scale, the parallel alignment of mountain-crossing grooves in Fig. 11 (arrows, C) suggests the grooves are not gravity-driven forms, which would have radial, not parallel, fall-lines descending the mountain-slopes. In context, this suggests that the parallel grooves represent glacially driven linear abrasion beneath formerly topography-inundating, sliding ice. The development of channel-like networks from parallel grooves, where topography is centripetally focussed (Fig. 11a, arrows D), suggests that liquid was produced in the subglacial environment and involved in groove incision, given the continuity from parallel grooves to convergent grooves to channels. This morphological continuum, therefore, represents a process continuum modulated by transitions between glacially driven stress and gravitational stress.

4.2.6. *Meso-scale subglacial meltwater channels*

A candidate subglacial channel is shown in part of the HiRISE anaglyph in Fig. 12, at the interface between the lineated surface near the northern margin of the LVF 2431 complex (Fig. 12a, region A) and a more densely cratered surface unit (Fig. 12a region B) to the north (Fig. 1 and Appendix S2.4 provide context). Reach S-S′ is 5.5 km in length, its mean width between channel shoulders is ~115 m and its *V-index* ranges from 0.1 to −0.063 (i.e. V-shaped). This channel reach appears first at the LVF terminus, in a shallow basin, and cuts across the flank of a hill (Fig. 12 at C), which closes the northern rim of the basin. The channel becomes less apparent (Fig. 12 at D) for 3.4 km (although possible traces of the channel remain apparent on the surface), before re-emerging along reach N-N′ (Fig. 12a, b). Reach N-N′ is 2.3 km long, has a mean width between shoulders of ~75 m and a *V-index* of −0.063 (i.e. V-shaped).

On the flank of hill C opposite the initial channel emergence at S (Fig. 12a), the terrain is incised by parallel NW-SE grooves (Fig. 12a between labels C and E). Planimetrically, the channel and grooves converge on the downslope centreline of hill C but the channel crosscuts the grooves. Reach N-N′ (detail in Fig. 12b) crosscuts another set of parallel grooves, these oriented NNE-SSW and, therefore, possibly associated with a viscous overflow from the large crater partly visible in Fig. 12a close to label B. Surface F (Fig. 12a) is subtly lineated, parallel to the NNE-SSW grooves, and is incised by a short channel.

4.2.6.1. Interpretation. The anaglyph suggests that the initial reach of the channel (Fig. 12a at S) is incised along an adverse slope, and that reach N-N′ crosscuts grooves, also initially along an adverse slope (Fig. 12 b). Arrowed labels X, Y and Z (Fig. 12a and Fig. 13) point to the locations of inflexions in the channel profile. X and Y are convex-up inflexions (not adverse undulations) in the curve along reach S-S′ (Fig. 13, profile a). With a total elevation change of 366 m from S-N′, the undulation at the head of S-S′ and, along reach N-N′, feature Z both have $\Psi = 0.02$ (Fig. 13, profile a). However, the incision of the channel into the substrate along reach N-N′ must have subdued the feature Z undulation (over time fluvial erosion would achieve a concave-down profile). Profile b in Fig. 13 was plotted immediately west of reach N-N′ and shows the topography that water flows would most likely have encountered at the start of the incision process. This profile indicates that water would have had to flow uphill for ~1.7 km to incise the channel as we now see it, ascending by 17 m ($\Psi = 0.05$).

The contours in Fig. 13c (HiRISE 2 m DEM, 20 m contour interval)

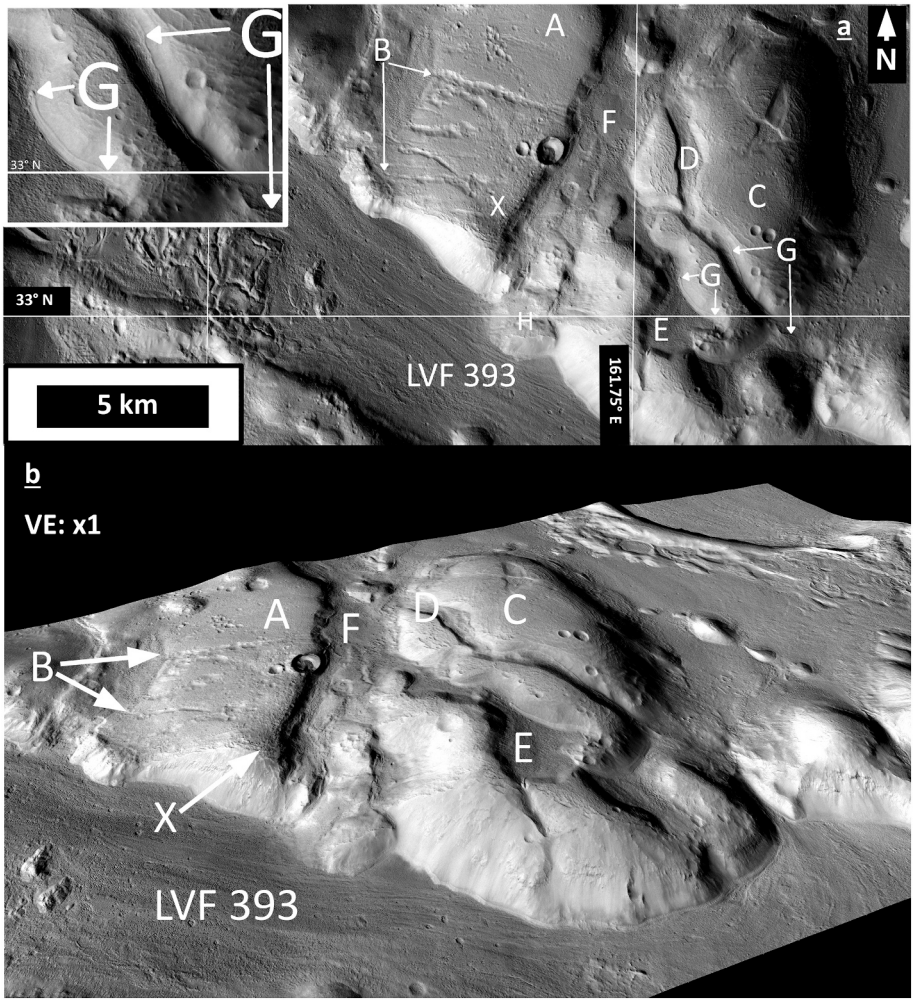

Fig. 10. (Panel a) Smoothed rock ramp (A) scored by long, narrow grooves (B), with first order, channel-like confluences. Dome-shaped rock platform (C) incised by troughs (D and E). Trough (F), bisects (A) and (C) and joins the LVF 393 trough at a hanging valley junction. The interface between F and ramp A is down-worn (at X) and funnels into the head of the southernmost channel-like groove (groove indicated by south pointing arrow from marker B). (G) MLR in D and E (inset panel, top-left corner of main panel a shows detail of these MLR). (H) outflow lobe from F into the LVF 393 trough. CTX image G23_027279_2132_XN_33N198W. (Panel b) CTX image over HRSC DEM showing topographic setting of landforms shown in panel: A (platform); B (groove assemblage); C (dome); F (trough); X down-worn interface between F and A, funnelling into B. Image credits: CTX image, NASA/JPL/MSSS;. HRSC DEM ESA/DLR/FU Berlin.

are congruent with the longitudinal profiles. Channel reach X-Y (Fig. 12a, Fig. 13a,c) is not contour-orthogonal but the grooves that this reach cross-cuts are (hence these grooves might be older gravity-driven channels similar to the channels at D in Fig. 11a). The reach between the contour closest to feature Z (−2520 m) and the −2540 m contour (Fig. 13b,c) also is not contour-orthogonal; the channel becomes contour-orthogonal downslope from the −2540 m contour. Hence, the contour lines support the indications from the longitudinal elevation profiles (in both contour deviation and profile undulation) that pumped flow, rather than only gravitational flow, was involved in the channel incision. Altogether, the measured characteristics of the channel (*V-index* $\leq$ 0.1, $\Psi > 0$, variation in channel-contour alignment) are consistent with hydraulic incision in a subglacial environment.

4.2.7. *Tunnel valleys*

Fig. 14a shows a channel-like form (D) of ~7 km length, sinuosity 1.1, width 0.8–1.2 km and mean depth ~ 30 m (mean w:d 37; d estimated from PEDR data, HRSC DEM data and shadow length cast by the western bank of both channels). Cross-sections V1 and V2 (Fig. 14b) have a *V-index* of 0.04 and − 0.019 (i.e. V-shaped). The longitudinal path of D (L-L') is convex-up (Fig. 14b, dotted trendline) and dominated by three adverse undulations, each with $\Psi > 0$: $\Psi(Z) = 0.22$; $\Psi(Y) = 0.05$; $\Psi(X) = 0.05$). The distal reach of D (downslope of *X*) contains a fill, incised by smaller (~50 m width), sinuous channels. D is part of a group of low sinuosity, high w:d channel-like forms (context, Appendix S2.10), including D* (Fig. 14a), which is largely occupied by a coarse-textured fill. Fig. 14 also shows giant (~1 km wide, ~2 km long), longitudinally asymmetric, positive relief forms (A) beside channel-like form D. The positive relief forms (A) are moulded into the downslope-distal surface of a smoothed platform (B), characterised by rimless craters, and bounded to the east by channel-like form D. The positive relief forms (A) are incised longitudinally by narrow grooves, and bounded around their steep (upslope-proximal) face and lateral margins by morphologically complementary, tapering depressions (C). More widely, the surfaces incised by forms D and A are densely incised by small channel-like forms (E), in particular joining D* with high confluence angles (Fig. 14a,b).

4.2.7.1. Interpretation. In the landscape context of Fig. 14a,b, the high w:d channel-like forms (D and D*), small channels (E) and asymmetric depression-bound positive relief forms (A) are all consistent with having been liquid-incised, albeit in different process environments. The *V-index* measures from two cross-sections of D (Fig. 14, V1, V2) are $\leq$0.1 and, therefore, consistent with fluvitile incision (Bouquety et al., 2019). However, the convex-up longitudinal profile of D and its $\Psi > 0$ undulations are not consistent with sub-aerial fluvial incision but, instead, with incision in a subglacial environment (Galofre et al., 2018). The small channels (E) suggest late-stage fluid flows with distributed sources, as opposed to earlier, larger episodes of erosion responsible for D and D*. The depression-bounded positive-relief forms (A) closely resemble *sichelwanne*. Described by Kor et al. (1991) and Shaw (2002), *sichelwanne* are hairpin-shaped shear-forms (s-forms), produced beneath sliding ice by highly erosive flows of subglacial meltwater or meltwater-sediment mixtures (slurries; cf. Meehan et al., 1997). S-form location is

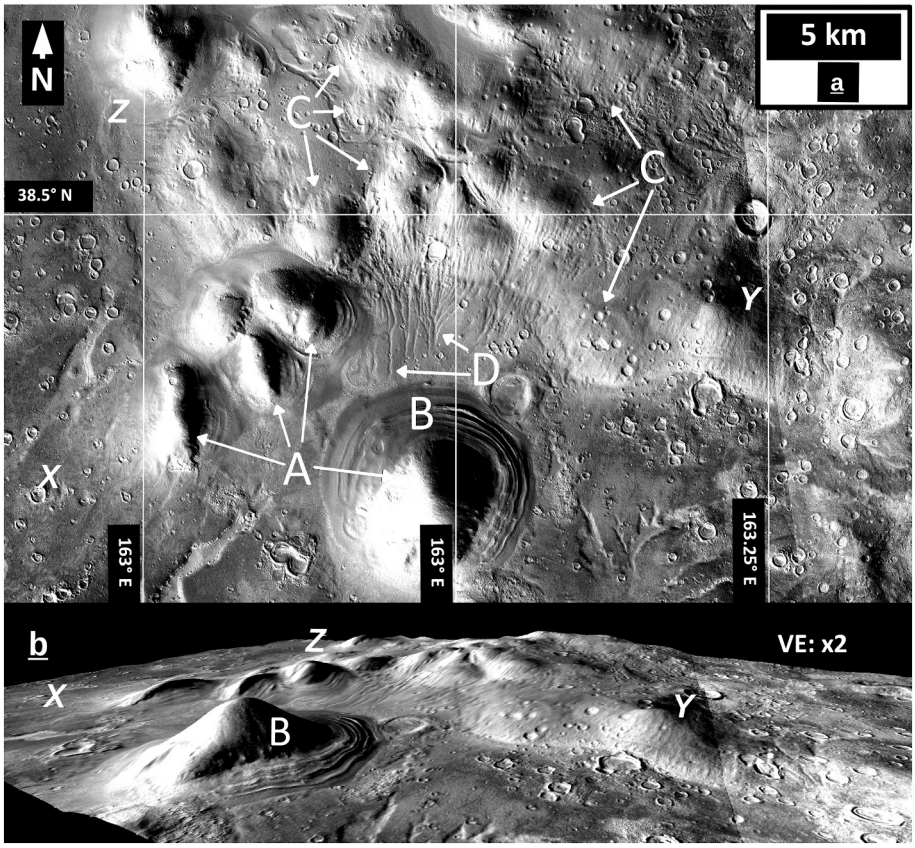

Fig. 11. (Panel a) Smoothed mountains (A) surrounded by lowland viscous forms, including prominent concentric viscous form (B). Mountains characterised by rounded summits, non-radial, "raked", grooves (C) and many rimless craters. Raked grooves converge downslope to channel-like forms where slopes become centripetal (D). Markers *X*, *Y*, *Z* are location references. (Panel b) DEM showing descending topographic sequence: raked upland summits; channel-like forms developed from grooves, where slopes are centripetal in middle elevations, and; viscous forms fringing the mountains. Markers *X*, *Y*, *Z* are location references with panel a. CTX image: G07_020778_2193_XI_39N197W. Image credit: NASA/JPL/MSSS. DEM: HRSC (data credit: ESA/DLR/FU Berlin).

not topographically controlled; they develop both in stoss-side and lee-side situations (Menzies and Shilts, 2002; Menzies and Shilts, 2002). In context with the s-form analogues, the channel-like forms D and D* (Fig. 14) have the scale, form and geometry of subglacial tunnel valleys (Cofaigh and C., 1996; Beaney, 2002; Lelandais et al., 2016; Livingstone and Clark, 2016). Tunnel valleys are elongated depressions, found close to former ice sheet margins, and have three diagnostic characteristics: they begin and end abruptly; their along-path width varies little as a function of down-channel distance, and; their floors are undulatory, with overdeepened reaches and adverse reaches. Generally, they are rectilinear to mildly sinuous in planform, aligned parallel to local ice flow indicators. They can be components of dendritic, anastomosed or braided channel networks. Cross-sections are U-shaped or V shaped, with steep sides and high width-to-depth ratios, reaching 50:1. These characteristics together, but particularly the presence of adverse reaches, indicate that tunnel valleys are products of incision by pressurized, subglacial water (Cofaigh and C., 1996; Beaney, 2002). All these characteristics are present in channel-like form D (in D*, the fill precludes reliable measurement of Ψ but the other tunnel valley characteristics are present). Given the contextual presence of the positive relief forms resembling *sichelwanne* (s-forms), we suggest the channel-like forms are strong tunnel valley candidates, representing a former warm-based subglacial zone. Alternatively, the channel-like forms could be glacially abraded troughs, incised, then filled, by sediment, or ice-sediment mixes, prior to late-stage incision of the smaller channel assemblage. Even if so, the candidate *sichelwanne* (s-forms) (and the grooves along them) are strongly suggestive of a wet, high shear, subglacial environment, possibly involving post-shear linear abrasion (with respect to the superimposed longitudinal grooves).

4.3. Summary and synthesis of landscape observations

The insights to the composition and structure of LDA 1694 (Fig. 2b) from SHARAD (Section 4.1.4, Fig. 3), together with its viscous flow characteristics, point conclusively to its glacial nature. The consilience between the flow structures of LDA 1694 and the other VFF in Phlegra Montes is strongly indicative of the other VFF being glaciers, not lithic or volcanic valley fills (cf. Byrne et al., 2013). In that context, LVF flow structures and forms, including various MLR forms (Fig. 4 and Fig. 8), correspond with the streamlining and development of stoss-to-lee asymmetry in the erosion (Fig. 8) of smooth platforms bypassed by extant LVF. The presence of MLR draped across streamlined platforms suggests that the thickness of these LVF was formerly sufficient to override the platforms. The consistent correspondence between LVF flow indicators and adjacent platform surface form suggests that the platform smoothness is primarily a product of subglacial scour, with local modification by abrasion, not simply a consequence of mantling. The observations and morphometrics presented in Section 4.2 (in the context of the extensive regional distribution of smoothed, grooved and raked terrain) point to a large proportion of the Phlegra Montes landscape being an assemblage of exposed, subglacially eroded surfaces. The exposure of these subglacial landforms points to a very significant deglaciation having taken place. Rounded, smoothed, km-scale mountaintops are common in Phlegra Montes, including many surrounded by extant LVF or LDA. Similarly, many passes between mountain domes, and forelands beyond them, are densely raked with parallel narrow grooves. Where slopes converge on constrictions between mountain domes, or in terminal basins at the foot of mountain-domed escarpments, grooves converging into arborescent networks of channel-like forms are very common (e.g. Fig. 11).

5. Discussion

5.1. Landform associations and environmental controls

In Phlegra Montes, narrow grooves consistently evolve downslope to

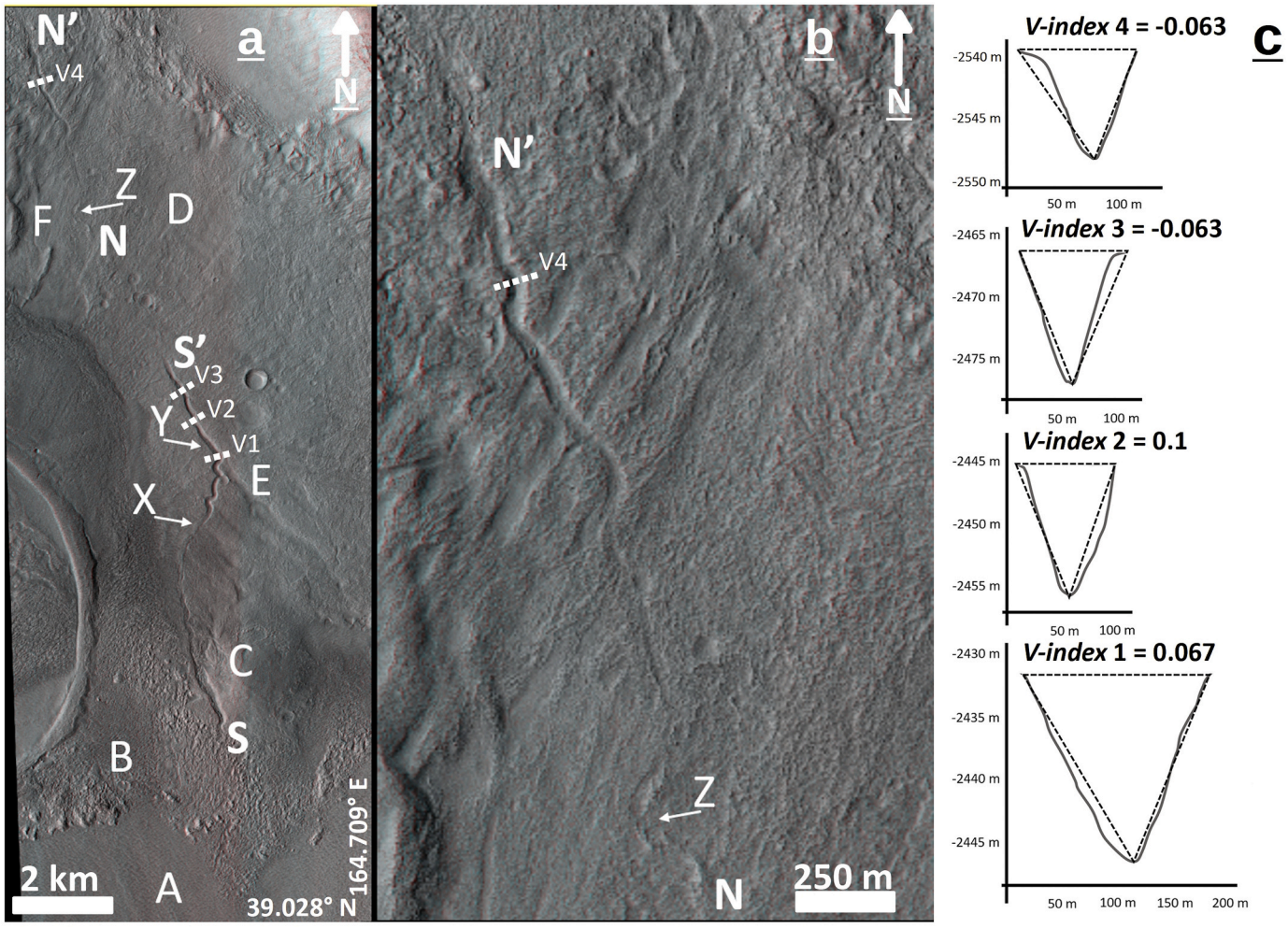

Fig. 12. (Panel a) S-S′ and N-N′ are reaches of a candidate subglacial channel. (A) lineated surface, part of the northern margin of LVF 4258 complex (Appendix S1). (B) More densely cratered surface unit to the north includes viscous crater fill/overspill and small LDA. (C) rounded hill with incised flank channel, reach S-S′. (D) terrain in which S-S′ becomes less apparent is characterised by concentric-ring craters, suggesting that S-S′ might continue beneath a thin icy unit. (E) parallel NW-SE grooves crosscut by S-S′. (F) Subtly lineated surface and second, small channel. Points X and Y (arrowed) are locations of channel profile convex-up inflexions shown in Fig. 13a. V1-V4 mark the locations of measured channel cross-sections. (Panel b) Detail of reach N-N′, including point Z (arrowed), where the channel profile becomes adverse (see Fig. 13b), marking the start of a convex-up undulation. (Panel c) Channel cross-sections V1-V4 with *V-index* measures; all are ≤0.1, hence V-shaped and consistent with fluviatile incision. HiRISE anaglyph ESP_052254_2195_ESP_052544_2195. Image credit: NASA/JPL/MSSS.

be replaced by sinuous, often networked, channel-like forms. Based on Earth analogues, these landforms could reflect a genetically associated trend, evolving from linear glacial abrasion to glaciofluvial incision. Linear grooves occur as parallel, diverging or converging sets, the arrangement depending on underlying relief and slope; the "raked" grooves in Fig. 11 are continuous for several kilometres, but also exhibit curvilinearity and convergence depending on contextual terrain slope and topographic constraint (see also Appendix S2.11). Parallel sets of raked grooves are consistent with linear abrasion by a liquid or slurry with no degrees of freedom to migrate laterally or fall under gravity, despite the present landscape showing no such constraint. Where parallel sets of grooves incise rounded mountain domes, the expected groove pattern for unconstrained liquid flows would be radial. This evidence for the grooves being produced by laterally constrained fluid abrasion is consistent with subglacial linear erosion. This interpretation is strengthened by the presence of the smooth, elongated, axially grooved positive relief forms within confining tapering depressions, including their contextual landform assemblage (Fig. 14a, b); high w:d channels, sinuous channels and channel networks (Fig. 14) are also consistent with having been liquid-incised in a subglacial setting. The high w:d channels (e.g. Fig. 14) have the scale, form and geometry of subglacial tunnel valleys (Livingstone and Clark, 2016) or abraded troughs containing a post-incision fill. The depression-bounded forms closely resemble *sichelwanne* (hairpin shaped s-forms) produced by highly erosive flows of subglacial meltwater or meltwater-sediment slurries (Kor et al., 1991; Shaw, 2002). If the smoothed mountain domes and grooves represent former subglacial scour and linear abrasion involving basal meltwater or meltwater-sediment slurries (Fig. 10), the channel-like networks (Fig. 11) could represent distal meltwater discharges, or discharges of the meltwater component of abrasive slurries. In that respect, the groove-channel landform assemblage would effectively map the glacial maximum configuration of a warm-based ice sheet system far larger, and more integrated, than the extant VFF of the region.

The occurrence of col-like passes occupied by VFF, and both morphologically complementary VFF-free passes and diffluent/transfluent outlets, are consistent with widespread linear erosion by formerly thicker and more extensive glaciers. This suggests that a period of significant deglaciation has occurred, following a regional glacial maximum (Baker and Head, 2015; cf. Brough et al., 2016). The distribution and elevations of channel heads is especially consistent with the wastage of montane LVF > 50 but not with LDA > 50. However, the LDA

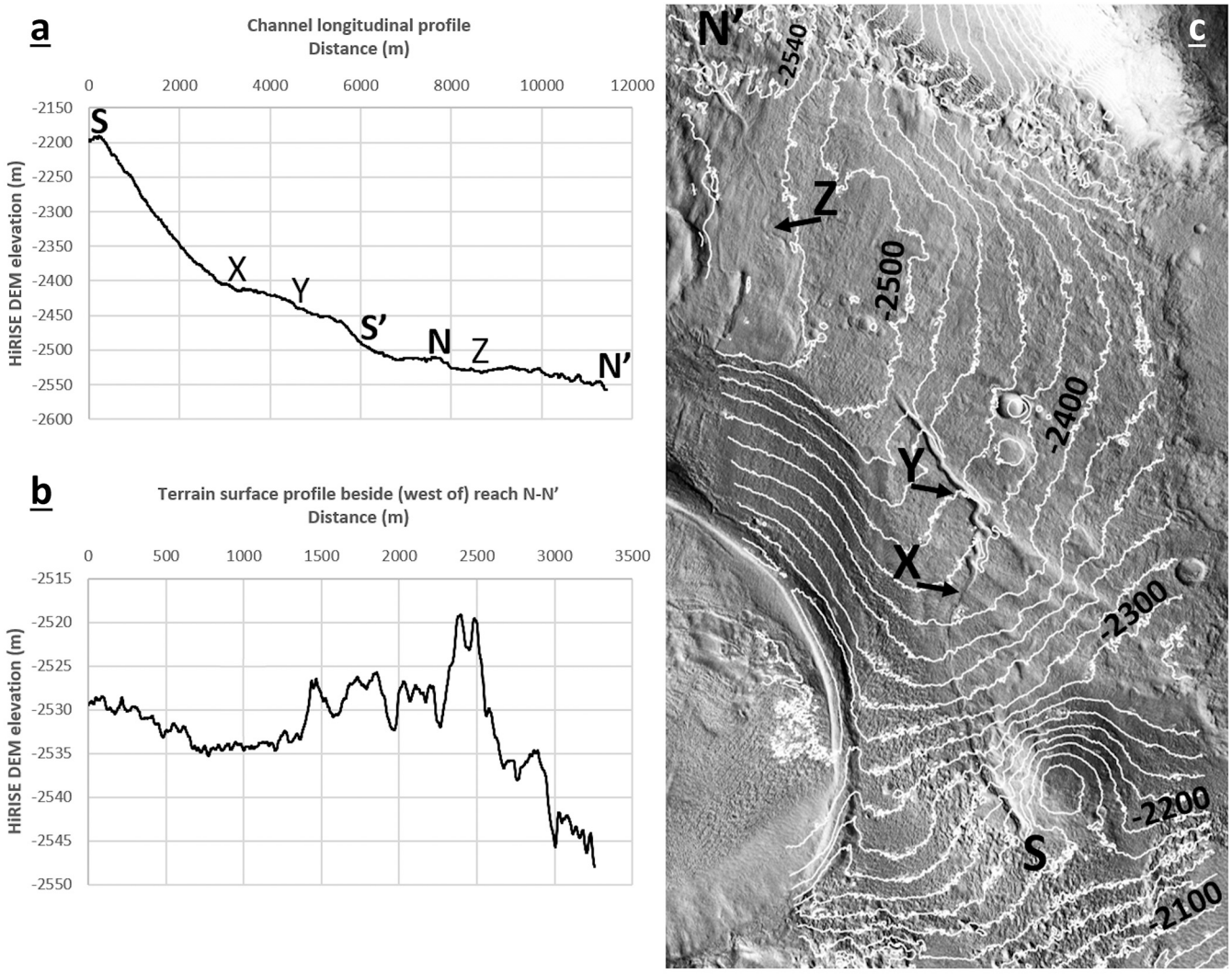

Fig. 13. (Curve a). Longitudinal profile of candidate subglacial channel. The total change in elevation (S-N′) is 366 m. The initial reach at S is an adverse undulation ($\Psi = 0.02$). Features X and Y are convex-up inflexions (not undulations) along reach S-S′. In reach N-N′, feature Z is an adverse undulation ($\Psi = 0.02$). (Curve b) The terrain profile immediately west of N-N′ indicates that water would have ascended by 17 m, over ~1.7 km ($\Psi = 0.05$), during the initial incision of the channel at Z. (Panel c) Contoured image (HiRISE 2 m DEM elevations, 20 m contour interval); channel reach X - Y and reach Z – N′ between the −2520 m and − 2540 m contour lines are not contour orthogonal. North is up. Scale can be judged by reference to the profiles. HiRISE DEM from stereo image pair ESP_052254_2195_ESP_052544_2195. Image credit: NASA/JPL/MSSS. DEM production: see Acknowledgements.

> 50 are generally lower in elevation than LVF > 50 (Appendix S2.2) and, based on adiabatic atmospheric warming, might be predicted to produce larger amounts of meltwater than LVF > 50. This apparently contradictory observation needs to be investigated further. A starting point lies in a comparison with glaciers on Earth that have termini spanning a restricted altitudinal range (i.e. hypsometrically bottom-heavy). These should be the most sensitive population to any change in ELA, due to adiabatic warming at lower elevations (Furbish and Andrews, 1984). In this respect, on Mars, on the basis of elevation, LDA (median MGE −2815 m; Appendix S2.2) might be predicted to be more sensitive than LVF (median MGE −2469; Appendix S2.2). However, the dry adiabatic lapse rate of the martian atmosphere is only 4.3 $K.km^{-1}$ (Leovy, 2001), in contrast to a value of ~10 $K.km^{-1}$ for Earth. Moreover, atmospheric dust on Mars reduces the effective adiabatic lapse rate to 2.5 $K.km^{-1}$ (Leovy, 2001). Fastook et al. (2008) determined that the absence of an effective adiabatic lapse rate on Mars means that sublimation diminishes less with increasing altitude than on Earth. Consequently, higher glaciers on Mars would be expected to have a reduced mass balance, due to persistent sublimation (Fastook et al., 2008). In conformity with this prediction, that mass balance on Mars should have an inverse relationship with elevation (positive mass balance at lower elevations but reducing, possibly becoming negative, at higher elevations), Phlegra Montes is characterised by bottom-heavy glacial systems (Appendix S2.2) that are overlooked by relict glacial landscapes at higher elevations. However, evidence of warm-based glaciation is common in these relict landscapes. This suggests that a warm-based phase of glaciation was succeeded by VFF wastage, particularly at higher elevations, dominated over time by sublimation. Other factors contributing to variation in VFF sensitivity could involve altitude variation in moisture-bearing wind direction, and both aspect and insolation-shadowing, particularly of generally low-lying LDA by large massifs. All these factors could contribute to the evolution of sub-regional climate and microclimate in Phlegra Montes but need to be investigated further. SHARAD results (Fig. 3), and complementary analysis of HiRISE imaging data (Appendix S2.3), indicate that LDA 1694 is an accumulation of nearly pure ice, up to ~390 m thick (average thickness ~ 200 m; Appendix S2.2), covered by a regolith layer (a rock glacier with up to 10% low density regolith by volume or 4% basaltic rock are other possible configurations). The regolith could have reduced the sensitivity of LDA 1694 to surface melt sufficiently for it to persist

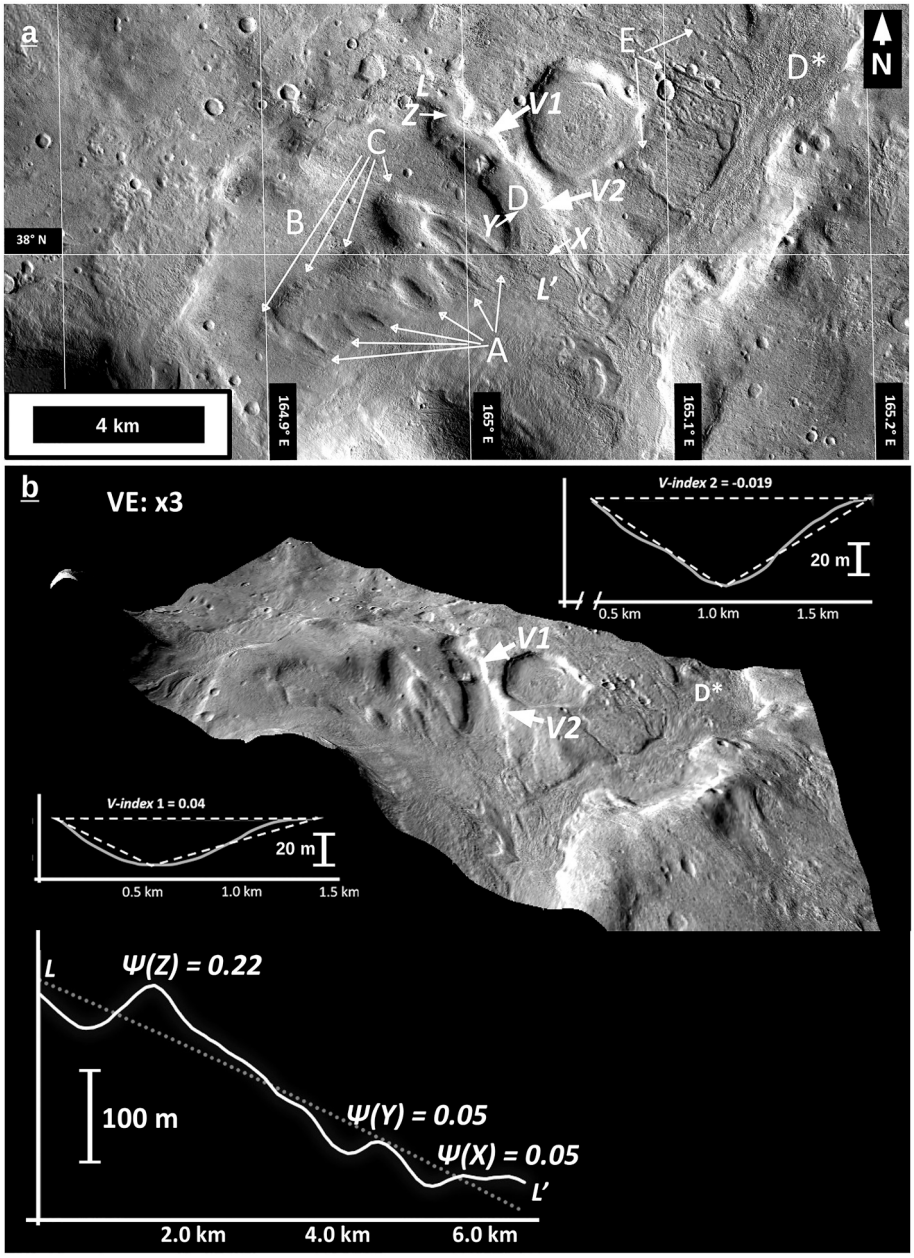

Fig. 14. (Panel a) Longitudinally asymmetric, positive relief forms (A) moulded into smoothed surface (B) and bounded by morphologically complementary depressions (C). Large, high w:d channels (D, D*) and smaller sinuous channels (E). (Panel b) DEM for topographic context, with V-index measures (V1, V2) and longitudinal profile L-L', including *Ψ(Z, Y and X)*. CTX image P17_007658_2175. Image credit: NASA/JPL/MSSS. HRSC DEM credit: ESA/DLR/FU Berlin.

through multiple obliquity cycles (Bramson et al., 2017). Unfortunately, the radar data (unaffected by topographic clutter) required to determine the debris cover and content (beyond probably thin surficial deposits resolvable in HiRISE imaging data) of LVF in Phlegra Montes are not yet available.

6. The possibility of subglacial erosion by dry based glaciers

Warm ice with basal meltwater deforms more easily and moves more rapidly than cold ice (without basal meltwater) due to basal sliding. In addition, warm ice entrains more debris and produces erosive meltwater discharges, due to pressure fluctuations induced by variable ice confinement. It is, therefore, more erosive than cold ice. Although cold based glaciers can achieve limited erosion (Cuffey et al., 2000; Hambrey and Fitzsimons, 2010), basal sliding owing to the presence of basal meltwater is required for glaciers to be regionally erosive. However, if sufficient dynamic basal pressure and/or strain heating is achieved at the base of very cold glaciers, melting can occur, giving rise to polythermal glaciers. These systems are typically frozen and dry-based around their thin margins but warm-based in their interiors or where they impinge on large bedrock obstacles. Polythermal glaciers move by basal sliding or, where their substrates have high porewater pressure, by subglacial deformation. Their drainage systems are mainly supraglacial and englacial, more rarely subglacial (Hambrey and Glasser, 2012). However, meltwater can penetrate cold-based margins at the base (Kavanaugh and Clarke 2001; Bingham et al. 2005 and 2006).

In Phlegra Montes, the macro-scale morphological evidence suggests that subglacial abrasion occurred across the region; cols, passes and crater rim breaches are overlooked by rounded, linearly abraded dome-like peaks and whalebacks. Sugden (1974) interpreted morphologically analogous landscapes on Earth as being indicative of basal sliding in limited contexts where local conditions allowed basal pressure melting.

Although cold-based glaciers in Antarctica have been observed to produce centimetre-scale erosional landforms (Atkins et al., 2002; Bockheim, 2010; Atkins and Dickinson, 2007), the kilometre-scale abrasion landforms and channels in Phlegra Montes dwarf them, making cold-based erosion alone an unlikely explanation of the landscape of Phlegra Montes. Hence, if the extant VFF of Phlegra Montes are presently cold-based, the abrasion landforms and channels visible beyond the VFF margins most likely represent a phase of expanded warm-based or polythermal glaciation.

7. Summary and conclusions

A total of >16,000 km^2 of VFF exceeding 50 km^2 have been mapped in Phlegra Montes (Fig. 1, Appendix S1). SHARAD data (and area-based thickness estimates in Appendix S2.2), indicate that LDA 1694 is the thickest regional VFF, at ~390 m (average thickness 200 m). Exposed former sub-glacial erosion surfaces and landforms morphologically and contextually analogous to landforms considered diagnostic of warm based glacial erosion on Earth (Glasser and Bennett, 2004) are common in the region. These landforms reflect a process continuum bracketed by wet-based areal scour and subglacial channel incision as endmembers. Intermediate processes involved linear abrasion, s-form erosion, groove incision and the development of distal channels from grooves. The extensive presence in Phlegra Montes of landforms considered indicative of warm based subglacial processes on Earth is, therefore, interpreted as evidence that subglacial abrasion occurred widely in Phlegra Montes. The interpretation of glacial wastage following warm based abrasion, supported by both erosional and depositional markers along the walls of troughs occupied by LVF, and both along and across abraded rock forms now exposed, means that the present VFF of Phlegra Montes do not represent the maximum extent of glaciation in the region. The incision of channels has been common in Phlegra Montes; both their geomorphology and context support the hypothesis that they formed in subglacial, ice contact and proximal ice marginal settings, prior to VFF retreat. Gallagher and Balme (2015) concluded that the presence in Phlegra Montes of an esker still physically associated with LVF 393, and its contextual landsystem, represents spatially limited warm-based conditions, associated with enhanced geothermal heating along a narrow but regionally extensive graben. Butcher et al. (2017) confirmed that the potential for subglacial melt induced solely by atmospheric heat, in the absence of sufficient geothermal heat flux and/or strain heating, is very unlikely. The Phlegra Montes esker remains an extremely rare landform but this paper has presented evidence of subglacial abrasion and channel incision consistent with the widespread action of warm-based glaciers in the region. Consequently, a better understanding of the thermal environment, both endogenic and exogenic, in which these glaciers operated is required to reconcile the landscape with the palaeoenvironmental contexts it represents. An environmental transition is strongly expressed by the regional geomorphology; a warm-based phase of glaciation, in which subglacial meltwater was produced and involved in distinctive landscape generation, was succeeded by VFF wastage, particularly at higher elevations and, therefore, probably dominated by sublimation (cf. Fastook et al., 2008).

Some individual landforms or landscapes that appear to be promising candidates for warm-based glacial erosion could be interpreted in a non-glacial paradigm. However, any such interpretation would ignore the total assemblage of landforms present in Phlegra Montes. Contextualized by extant VFF, and by reference to diagnostic morphological analogues on Earth (Glasser and Bennett, 2004), the landform assemblage of Phlegra Montes can be interpreted as a complete and compelling set of morphological indicators of warm based glaciation.

Funding acknowledgement

FEGB is part of the PALGLAC research team supported by the European Research Council (ERC) under the European Union's Horizon 2020 research and innovation programme (Grant agreement No. 787263). FEGB also acknowledges funding from the Science and Technology Facilities Council (STFC) grant ST/N50421X/1.

Declaration of Competing Interest

None.

Acknowledgements

The authors are grateful to the two anonymous reviewers of this paper, who made significant contributions through their insights and suggestions; their work is much appreciated.

The authors acknowledge the work of Joel Davis in kindly producing the HiRISE DEM used to generate data presented in Fig. 12 and Fig. 13. The authors also acknowledge Susan Conway, who made valuable contributions to discussions during the progress of this work.

Appendix A. Supplementary data

Supplementary data to this article can be found online at https://doi.org/10.1016/j.icarus.2020.114173.

References

Alley, R.B., Cuffey, K.M., Zoet, L.K., 2019. Glacial erosion: status and outlook. Ann. Glaciol. 1–13. https://doi.org/10.1017/aog.2019.38.

Aniya, M., Welch, R., 1981. Morphometric analyses of Antarctic cirques from photogrammetric measurements. Geografiska Annaler Series A Phys. Geogr. 63 (1–2), 41–53. https://doi.org/10.1080/04353676.1981.11880017.

Atkins, C.B., Dickinson, W.W., 2007. Landscape modification by meltwater channels at margins of cold-based glaciers, Dry Valleys, Antarctica. Boreas 36, 47–55. https://doi.org/10.1111/j.1502-3885.2007.tb01179.x.

Atkins, C.B., Barrett, P.J., Hicock, S.R., 2002. Cold glaciers erode and deposit: evidence from Allan Hills, Antarctica. Geology 30 (7), 659–662. https://doi.org/10.1130/0091-7613(2002)030<0659:CGEADE>2.0.CO;2.

Baker, D.M.H., Carter, L.M., 2019. Probing supraglacial debris on Mars 1: sources, thickness, and stratigraphy. Icarus 319, 745–769. https://doi.org/10.1016/j.icarus.2018.09.001.

Baker, D.M.H., Head, J.W., 2015. Extensive middle Amazonian mantling of debris aprons and plains in Deuteronilus Mensae, Mars: implications for the record of mid-latitude glaciation. Icarus 260, 269–288. https://doi.org/10.1016/j.icarus.2015.06.036.

Barr, I.D., Spagnolo, M., 2015. Glacial cirques as palaeoenvironmental indicators: their potential and limitations. Earth Sci. Rev. 151, 48–78. https://doi.org/10.1016/j.earscirev.2015.10.004.

Barr, I., Ely, J., Spagnolo, M., Evans, I., Tomkins, M., 2019. The dynamics of mountain erosion: cirque growth slows as landscapes age. Earth Surf. Process. Landf. https://doi.org/10.1002/esp.4688.

Beaney, C.L., 2002. Tunnel channels in Southeast Alberta, Canada. Quat. Int. 90 (1), 67–74. https://doi.org/10.1016/S1040-6182(01)00093-3.

Bingham, R.G., Nienow, P.W., Sharp, M.J., Boon, S., 2005. Subglacial drainage processes at a High Arctic polythermal valley glacier. J. Glaciol. 51, 15–24.

Bingham, R.G., Nienow, P.W., Sharp, M.J., Copland, L., 2006. Hydrology and dynamics of a polythermal (mostly cold) High Arctic glacier. Earth Surf. Process. Landforms 31, 1463–1479. https://doi.org/10.1002/esp.1374.

Bockheim, J.G., 2010. Soil preservation and ventifact recycling from dry-based glaciers in Antarctica. Antarct. Sci. 22 (4), 409–417. https://doi.org/10.1017/S0954102010000167.

Bouquety, A., Sejourné, A., Costard, F., Mercier, D., Bouley, S., 2019. (2019). Morphometric evidence of 3.6 Ga glacial valleys and glacial cirques in martian highlands: south of Terra Sabaea. Geomorphology 334, 91–111. https://doi.org/10.1016/j.geomorph.2019.02.022.

Bramson, A.M., Byrne, S., Putzig, N.E., Sutton, S., Plaut, J.J., Brothers, T.C., Holt, J.W., 2015. Widespread excess ice in Arcadia Planitia, Mars. Geophys. Res. Lett. 42 https://doi.org/10.1002/2015GL064844, 2015GL064844.

Bramson, A.M., Byrne, S., Bapst, J., 2017. Preservation of midlatitude ice sheets on Mars. J. Geophys. Res. Planets 122, 2250–2266.

Brough, S., Hubbard, B., Hubbard, A., 2016. Former extent of glacier-like forms on Mars. Icarus 274, 37–49. https://doi.org/10.1016/j.icarus.2016.03.006.

Butcher, F.E.G., Balme, M.R., Gallagher, C., Arnold, N.S., Conway, S.J., Hagermann, A., Lewis, S.R., 2017. Recent basal melting of a mid-latitude glacier on Mars. J. Geophys. Res. Planets 122, 2445–2468. https://doi.org/10.1002/2017JE005434.

Byrne, P.K., Klimczak, C., Williams, D.A., Hurwitz, D.M., Solomon, S.C., Head, J.W., Preusker, F., Oberst, J., 2013. An assemblage of lava flow features on mercury. J. Geophys. Res. Planets 118, 1303–1322. https://doi.org/10.1002/jgre.20052.

Carr, M.H., 2006. The Surface of Mars. Cambridge University Press, 307 pp.

Close, M., 1867. Notes on the general glaciation of Ireland. Royal Geol. Soc. Ireland J. 1, 207–242.
Cofaigh, Ó., C., 1996. Tunnel valley genesis. Prog. Phys. Geogr. 20 (1), 1–19. https://doi.org/10.1177/030913339602000101.
Conway, S.J., Butcher, F.E.G., de Haas, T., Deijns, A.A.J., Grindrod, P.M., Davis, J.M., 2018. Glacial and gully erosion on Mars: A terrestrial perspective. Geomorphology 318 (1), 26–57.
Cuffey, K., Conway, H., Gades, A., Hallet, B., Lorrain, R., Severinghaus, J., Steig, E., Vaughn, B., White, J., 2000. Entrainment at cold glacier beds. Geology 28, 351–354. https://doi.org/10.1130/0091-7613(2000)28<351:EACGB>2.0.CO;2.
Dickson, J., et al., 2009. Kilometer-thick ice accumulation and glaciation in the northern mid-latitudes of Mars: evidence for crater-filling events in the late Amazonian at the Phlegra Montes. Earth Planet. Sci. Lett. 294 (2010), 332–342.
Evans, I.S., Cox, N.J., 2017. Comparability of cirque size and shape measures between regions and between researchers, *Zeitschrift für Geomorphologie*. Supplementary Issues 61 (2), 81–103.
Eyles, N., 1983. Glacial Geology. In: An Introduction for Engineers and Earth Scientists. Oxford, Pergamon Press, p. 409. ISBN 0 08 030263 7.
Fassett, C.I., Levy, J.S., Dickson, J.L., Head, J.W., 2014. An extended period of episodic northern mid-latitude glaciation on Mars during the middle to late Amazonian: implications for long-term obliquity history. Geology 42, 763–766. https://doi.org/10.1130/G35798.1.
Fastook, J., Head, J., Marchant, D., Forget, F., 2008. Tropical mountain glaciers on Mars: altitude-dependence of ice accumulation, accumulation conditions, formation times, glacier dynamics, and implications for planetary spin-axis/orbital history. Icarus 198, 305–317. https://doi.org/10.1016/j.icarus.2008.08.008.
Fastook, J.L., Head, J.W., Marchant, D.R., 2014. Formation of lobate debris aprons on Mars: assessment of regional ice sheet collapse and debris-cover armouring. Icarus 228, 54–63. https://doi.org/10.1016/j.icarus.2013.09.025.
Fergason, R.L., Hare, T.M., Laura, J., 2018. HRSC and MOLA Blended Digital Elevation Model at 200m v2, *Astrogeology PDS Annex*. U.S. Geological Survey. http://bit.ly/HRSC_MOLA_Blend_v0.
Furbish, D.J., Andrews, J.T., 1984. The use of hypsometry to indicate long-term stability and response of valley glaciers to changes in mass transfer. J. Glaciol. 30 (105), 199–211.
Gallagher, C., Balme, M., 2015. Eskers in a complete, wet-based glacial system in the Phlegra Montes region, Mars. Earth Planet. Sci. Lett. 431, 96–109.
Galofre, A.G., Jellinek, A.M., Osinski, G.R., Zanetti, M., Antero Kukko, A., 2018. Subglacial drainage patterns of Devon Island, Canada: detailed comparison of rivers and subglacial meltwater channels. Cryosphere 12, 1461–1478. https://doi.org/10.5194/tc-12-1461-2018.
Glasser, N.F., Bennett, M.R., 2004. Glacial erosional landforms: origins and significance for Palaeoglaciology. Prog. Phys. Geogr. 28 (1), 43–75.
Golledge, N.R., Stoker, M.S., 2006. A palaeo-ice stream of the British ice sheet in eastern Scotland. Boreas 35, 231–243. https://doi.org/10.1111/j.1502-3885.2006.tb01153.x.
Grima, C., Kofman, W., Mouginot, J., Phillips, R.J., Hérique, A., Biccari, D., Seu, R., Cutigni, M., 2009. North polar deposits of Mars: extreme purity of the water ice. Geophys. Res. Lett. 36, L03203.
Hallet, B., 1996. Glacial quarrying: a simple theoretical model. Ann. Glaciol. 22, 1–8. https://doi.org/10.3189/1996AoG22-1-1-8.
Hambrey, M., 1994. Glacial Environments. UBC Press, p. 304.
Hambrey, M.J., Fitzsimons, S.J., 2010. Development of sediment–landform associations at cold glacier margins, Dry Valleys, Antarctica. Sedimentology 57 (3), 857–882. https://doi.org/10.1111/j.1365-3091.2009.01123.x.
Hambrey, M.J., Glasser, N.F., 2012. Discriminating glacier thermal and dynamic regimes in the sedimentary record. Sediment. Geol. 251–252 (15), 1–33. https://doi.org/10.1016/j.sedgeo.2012.01.008.
Head, J., Marchant, D.R., Agnew, M.C., Fassett, C.I., Kreslavsky, M.A., 2006. Extensive valley glacier deposits in the northern mid-latitudes of Mars: evidence for late Amazonian obliquity-driven climate change. Earth Planet. Sci. Lett. 241 (3–4), 663–671. https://doi.org/10.1016/j.epsl.2005.11.016.
Head, J.W., Marchant, D.R., Dickson, J.L., Kress, A.M., Baker, D.M., 2010. Northern mid-latitude glaciation in the late Amazonian period of Mars: criteria for the recognition of debris-covered glacier and valley glacier landsystem deposits. Earth Planet. Sci. Lett. 294 (3–4), 306–320. https://doi.org/10.1016/j.epsl.2009.06.041.
Hirano, M., Aniya, M., 1988. A rational explanation of cross-profile morphology for glacial valleys and of glacial valley development. Earth Surf. Process. Landf. 13, 707–716. https://doi.org/10.1002/esp.3290130805.
Holt, J.W., Safaeinili, A., Plaut, J.J., Head, J.W., Phillips, R.J., Seu, R., Kempf, S.D., Choudhary, P., Young, D.A., Putzig, N.E., Biccari, D., Gim, Y., 2008. Radar sounding evidence for buried glaciers in the southern mid-latitudes of Mars. Science 322, 1235–1238.
Hubbard, B., Milliken, R.E., Kargel, J.S., Limaye, A., Souness, C., 2011. Geomorphological characterisation and interpretation of a mid-latitude glacier-like form: Hellas Planitia, Mars. Icarus 211, 330–346.
Hubbard, B., Souness, C., Brough, S., 2014. Glacier-like forms on Mars. Cryosphere 8, 2047–2061. https://doi.org/10.5194/tc-8-2047-2014.
Karlsson, N.B., Schmidt, L.S., Hvidberg, C.S., 2015. Volume of Martian midlatitude glaciers from radar observations and ice flow modeling. Geophys. Res. Lett. 42, 2627–2633. https://doi.org/10.1002/2015GL063219.
Kavanaugh, J.L., Clarke, G.K.C., 2001. Abrupt glacier motion and reorganization of basal shear stress following the establishment of a connected drainage system. J. Glaciol. 47 (158), 472–480.
Kochel, R.C., Peake, R.T., 1984. Quantification of waste morphology in Martian fretted terrains, Proc. Lunar Planet. Sci. Conf., 15th, Part 1. J. Geophys. Res. 89 suppl., C336–C350.
Kor, P.S.G., Shaw, J., Sharp, D.R., 1991. Erosion of bedrock by subglacial meltwater, Georgian Bay, Ontario: a regional view. Can. J. Earth Sci. 28, 623–642.
Lelandais, T., Mourgues Ravier, É., Pochat, S., Strzerzynski, P., Bourgeois, O., 2016. Experimental modeling of pressurized subglacial water flow: implications for tunnel valley formation. J. Geophys. Res. Earth Surf. 121, 2022–2041. https://doi.org/10.1002/2016JF003957.
Leovy, C., 2001. Weather and climate on Mars. Nature 412, 245–249. https://doi.org/10.1038/35084192.
Levy, J.S., Fassett, C.I., Head, J.W., Schwartz, C., Watters, J.L., 2014. Sequestered glacial ice contribution to the global Martian water budget: geometric constraints on the volume of remnant, midlatitude debris-covered glaciers. J. Geophys. Res. Planets 119, 2188–2196. https://doi.org/10.1002/2014JE004685.
Lewis, W.V., 1949. Glacial movement by rotational slipping. Geogr. Ann. 31 (1–4), 146–158. https://doi.org/10.1080/20014422.1949.11880800.
Livingstone, S.J., Clark, C.D., 2016. Morphological properties of tunnel valleys of the southern sector of the Laurentide ice sheet and implications for their formation. Earth Surf. Dynam. 4, 567–589. https://doi.org/10.5194/esurf-4-567-2016.
Malin, M.C., Bell, J.F., Cantor, Bruce A., Caplinger, M.A., Calvin, Wendy M., Clancy, R. Todd, Edgett, K.S., Edwards, Lawrence, Haberle, R.M., James, Philip B., Lee, S.W., Ravine, M.A., Thomas, Peter C., Wolff, M.J., 2007. Context Camera Investigation on board the Mars Reconnaissance Orbiter. J. Geophys. Res. 112 https://doi.org/10.1029/2006JE002808. E5, E05S04.
McEwen, A.S., et al., 2007. Mars Reconnaissance Orbiter's High Resolution Imaging Science Experiment (HiRISE). J. Geophys. Res. 112 https://doi.org/10.1029/2005JE002605. E05S02.
Meehan, R.T., Warren, W.P., Gallagher, C.J., 1997. The sedimentology of a late Pleistocene drumlin near Kingscourt, Ireland. Sediment. Geol. 111 (1–4), 91–105.
Menzies, J., Shilts, W.W., 2002. Subglacial environments. In: Menzies, J. (Ed.), Modern and Past Glacial Environments. Butterworth-Heinemann, Oxford, pp. 183–278.
Milliken, R.E., Mustard, J.F., Goldsby, D.L., 2003. Viscous flow features on the surface of Mars: observations from high-resolution Mars orbiter camera (MOC) images. J. Geophys. Res. 108 https://doi.org/10.1029/2002JE002005.
Neukum, G., Jaumann, R., the HRSC Co-Investigator and Experiment Team, 2004. HRSC: The high resolution stereo camera of Mars express. In: Wilson, A. (Ed.), Mars Express: The Scientific Payload. ESA, Noordwijk, The Netherlands, pp. 17–35. https://www.esa.int/esapub/sp/sp1240/sp1240web.pdf.
Parsons, A.M., et al., 2011. Active neutron and gamma-ray instrumentation for in situ planetary science applications. Nucl. Instrum. Methods Phys. Res., Sect. A 652, 674–679.
Petersen, E.I., Holt, J.W., Levy, J.S., 2018. High ice purity of martian lobate debris aprons at the regional scale: Evidence from an orbital radar sounding survey in Deuteronilus and Protonilus Mensae. Geophys. Res. Lett. 45, 11,595–11,604. https://doi.org/10.1029/2018GL079759.
Pierce, T.L., Crown, D.A., 2003. Morphologic and topographic analyses of debris aprons in the eastern Hellas region, Mars. Icarus 163 (1), 46–65.
Plaut, J.J., Picardi, G., Safaeinili, A., Ivanov, A.B., Milkovich, S.M., Cicchetti, A., Kofman, W., Mouginot, J., Farrell, W.M., Phillips, R.J., Clifford, S.M., Frigeri, A., Orosei, R., Federico, C., Williams, I.P., Gurnett, D.A., Nielsen, E., Hagfors, T., Heggy, E., Stofan, E.R., Plettemeier, D., Watters, T.R., Leuschen, C.J., Edenhofer, P., 2007. Subsurface radar sounding of the south polar layered deposits of Mars. Science 316, 92–95. https://doi.org/10.1126/science.1139672.
Plaut, J.J., Safaeinili, A., Holt, J.W., Phillips, R.J., Head III, J.W., Seu, R., Putzig, N.E., Frigeri, A., 2009. Radar evidence for ice in lobate debris aprons in the midnorthern latitudes of Mars. Geophys. Res. Lett. 36, L02203 https://doi.org/10.1029/2008GL036379.
Robbins, S.J., Hynek, B.M., 2012. A new global database of Mars impact craters ≥1 km: 1. Database creation, properties, and parameters. J. Geophys. Res. 117 https://doi.org/10.1029/2011JE003966. E05004.
Seu, R., Phillips, R.J., Biccari, D., Orosei, R., Masdea, A., Picardi, G., Safaeinili, A., Campbell, B.A., Plaut, J.J., Marinangeli, L., 2007. SHARAD sounding radar on the Mars Reconnaissance Orbiter. J. Geophys. Res. 112. E05S05.
Shaw, J., 2002. The meltwater hypothesis for subglacial bedforms. Quat. Int. 90, 5–22.
Smith, D.E., Zuber, M.T., Frey, H.V., Garvin, J.B., Head, J.W., Muhleman, D.O., Pettengill, G.H., Phillips, R.J., Solomon, S.C., Zwally, H.J., 2001. Mars orbiter laser altimeter: experiment summary after the first year of global mapping of Mars (paper 2000JE001364). J. Geophys. Res. 106, 23–689.
Souness, C., Hubbard, B., Milliken, R.E., Quincey, D., 2012. An inventory and population-scale analysis of Martian glacier-like forms. Icarus 217, 243–255.
Squyres, S.W., 1979. The distribution of lobate debris aprons and similar flows on Mars. J. Geophys. Res. 84, 8087–8096.
Sugden, D., 1974. Landscapes of glacial erosion in Greenland and their relationship to ice, topographic and bedrock conditions, 7. Institute of British Geographers Special Publication, pp. 177–195.
Tanaka, K.L., Skinner Jr., J.A., Dohm, J.M., Irwin III, R.P., Kolb, E.J., Fortezzo, C.M., Platz, T., Michael, G.G., Hare, T.M., 2014. Geologic map of Mars: U.S. Geological Survey Scientific Investigations Map 3292, scale 1:20,000,000, pamphlet, p. 43. https://doi.org/10.3133/sim3292.
Zimmer, P.D., Gabet, E.J., 2018. Assessing glacial modification of bedrock valleys using a novel approach. Geomorphology 318, 336–347. https://doi.org/10.1016/j.geomorph.2018.06.021.